

# We are IntechOpen, the world's leading publisher of Open Access books Built by scientists, for scientists

6,900

Open access books available

186,000

International authors and editors

200M

Downloads

Our authors are among the

154

Countries delivered to

TOP 1%

most cited scientists

12.2%

Contributors from top 500 universities



WEB OF SCIENCE™

Selection of our books indexed in the Book Citation Index  
in Web of Science™ Core Collection (BKCI)

Interested in publishing with us?  
Contact [book.department@intechopen.com](mailto:book.department@intechopen.com)

Numbers displayed above are based on latest data collected.  
For more information visit [www.intechopen.com](http://www.intechopen.com)



# Germanium-on-Silicon for Integrated Silicon Photonics

Xiaochen Sun

*Massachusetts Institute of Technology*  
USA

## 1. Introduction

To meet the unprecedented demands for data transmission speed and bandwidth silicon integrated photonics that can generate, modulate, process and detect light signals is being developed. Integrated silicon photonics that can be built using existing CMOS fabrication facilities offers the tantalizing prospect of a scalable and cost-efficient solution to replace electrical interconnects. Silicon, together with commonly used dielectric materials in CMOS processes such as silicon dioxide, is a great material system for optical confinement and wave transmission in near infrared range. However, silicon is not a good choice for active photonic devices due to its transparency in such wavelength range. Germanium and GeSi alloy, the materials that have long been adopted to improve the performance of silicon transistors in many ways, have been showing their potential as the building blocks of such active integrated optical devices. This chapter discusses the research of using germanium and GeSi for silicon-integrated photodetection and light source in the contexts of material physics and growth, device design and fabrication.

This introduction section briefly introduces the background of integrated silicon photonics and some germanium properties which are important for photonic applications. Next section focuses on waveguide-integrated germanium photodetectors which can readily be integrated with silicon waveguide on mature silicon or silicon-on-insulator (SOI) platform. The physics and design considerations of these devices are presented with details. The fabrication processes of these devices are also discussed with some extent. Next section includes a newly developed field that using germanium for light sources in silicon photonics applications such as light-emitting-diodes (LEDs) and lasers. There has been a few breakthroughs in this topic including the author's work of epitaxial germanium LEDs and optically pumped lasers operating at room temperature. The physics of this unusual concept of using indirect band gap material for light emission is discussed in details and some important results are presented.

### 1.1 Integrated silicon photonics

Silicon integrated circuits (ICs) had been developed in an extraordinary pace for almost four decades before 2005. It is known as Moore's law that the number of transistors in an integrated circuit doubles roughly every eighteen months (Moore, 1965). The scalability is the main reason of the tremendous success of many silicon IC based technologies (Haensch et al., 2006), such as silicon complimentary metal oxide semiconductor (Si-CMOS) technology.

The scalability of Si-CMOS technology is not only about the shrinkage of the dimensions of the devices, but also a number of other factors for maintaining the power density while boosting the performance. However, many issues against further scaling have been found including applied voltage barrier (threshold voltage) and passive component heating due to sub-threshold leakage current. In 2005, "for the first time in thirty five years, the clock speed of the fastest commercial computer chips has not increased" (Muller, 2005) because of the above reasons.

In order to solve these problems in data transmission speed scaling and passive component heat dissipation, optical interconnects relying on silicon photonics are proposed as a promising solution. Silicon photonics offers a platform for the monolithic integration of optics and microelectronics on the same silicon chips (Lipson, 2004), aiming for many applications including the optical interconnects (Haurylau et al., 2006). At present, electrical circuit speed or propagation delay is limited by interconnect RC delay which increases with the scaling of device dimensions. Optical interconnects which use photon as information carrier are not subject to the RC delay in the first place. The weak electrical interaction between photons and guiding media inherently minimize heat generation in propagation. The interaction among photons is also weak at lower optical power so that multiple transmission using different wavelengths can co-exist in the same propagation channel. This wavelength multiplexing (WDM) technique dramatically increase the aggregated bandwidth of the transmission system. To achieve such optical interconnects using compatible silicon processing techniques is the major task of monolithic integrated silicon photonics (Aicher & Habberger, 1999; O'Connor et al., 2007; O'Connor et al., 2006). The compatibility with silicon enables a cost-effective, scalable and manufacturable solution for implementing silicon photonics. To address its importance and rapid growth, a roadmap of silicon photonics has been developed by academic and industrial professionals and released on a yearly basis (Kirchain & Kimerling, 2007).

## 1.2 Germanium epitaxy on silicon

The world's first transistor is made from Germanium by John Bardeen, Walter Brattain and William Shockley at Bell Labs in December, 1947. Beginning with this invention, a revolution of semiconductor electronics quickly started and have profoundly changed our life in many ways. But germanium, the first used semiconductor material, soon gave its crown to another semiconductor in the same elementary group - silicon - in this great revolution. Silicon has superior properties than germanium in many ways: chemical and mechanical stability, stable oxides and etc. Based on silicon, integrated circuit (IC) was realized and appeared in numerous electronic devices that we use and carry everyday.

Silicon was so successful that germanium was forgotten by most researchers for decades soon after the first silicon transistor was invented and commercialized from Texas Instrument in 1952. However, germanium has its own advantages, e.g. higher carrier mobility than silicon, thereby some researchers investigated ways to integrate germanium on silicon substrates. As semiconductor devices generally require single crystalline germanium thin films, the attempts of heterogeneous epitaxy of germanium on silicon emerged. People soon found a great difficulty of growing germanium thicker than its critical thickness because there is 4% mismatch between the lattice constants of germanium and silicon. Although the earliest work of the epitaxy of germanium-silicon (GeSi) alloy on silicon dates back to 1962 (Miller & Grieco, 1962), good quality pure germanium films or high germanium content GeSi films have been

grown on silicon since late 1970s after the invention of molecular beam epitaxy (MBE) (Bean et al., 1984; Garozzo et al., 1982; Kasper & Herzog, 1977; Tsaur et al., 1981).

Despite the importance of the studies of germanium epitaxy by MBE, it is recognized by many researchers that MBE is not likely to be a good choice for massive device manufacturing. The complexity of MBE equipment and the low yield of single wafer MBE process eventually gave way to chemical vapor deposition (CVD) for growing germanium and GeSi films on silicon substrate. A variety of CVD growth techniques have been developed for germanium and GeSi epitaxy since 1980s and the crystalline quality is equal to, if not better than, what can be achieved in MBE process.

The development of germanium and GeSi CVD epitaxy followed the work of CVD silicon epitaxy demanded by advanced metal-oxide-semiconductor field-effect transistor (MOSFET) devices. Like silicon epitaxy, early GeSi epitaxy in CVD systems was performed at atmospheric pressure. This type of growth usually requires a hydrogen prebake with an option of hydrochloride (HCl) vapor etch at very high temperature ( $>1100^{\circ}\text{C}$ ) to volatilize or dissolve native  $\text{SiO}_2$  or carbon on the silicon surface (Raider et al., 1975; Vossen et al., 1984). The growth temperature is carefully chosen (e.g. around  $800^{\circ}\text{C}$ ) to balance between a reasonable germanium growth rate and the prevention of relaxation of metastable strained layer. A typical CVD reactor of such kind used by some researchers for GeSi growth (Kamins & Meyer, 1991) is made by ASM International. Atmospheric pressure CVD has insurmountable shortcomings which make it less popular in growing high quality silicon and germanium epitaxial films nowadays. The atmospheric pressure chamber condition can not avoid impurities contaminations from ambient and the need for very high temperature bake and growth causes autodoping issue, a phenomenon where doped regions existent in a substrate transfer substantial amounts of dopant into the epitaxial layer.

To overcome these shortcomings, ultra-high vacuum chemical vapor deposition (UHVCVD) was introduced by Meyerson and co-workers at IBM T. J. Watson Research Center in 1986 (Meyerson, 1986). In a UHVCVD system, the base pressure of the chamber is usually in the range of  $10^{-8} \sim 10^{-9}$  torr when idling and  $10^{-3}$  torr during growth. At this ultra high vacuum environment, the contamination can be well controlled at a very low level. For example, the system induced background partial pressure of contaminants such as water vapor, oxygen, and hydrocarbons is limited to values in the range of  $10^{-11}$  torr (Meyerson, 1992). As a result of the superior condition of ambient and substrate surface, the germanium and GeSi epitaxial growth is performed at relatively low temperatures ( $400\sim 700^{\circ}\text{C}$ ) without requiring extensive high temperature hydrogen pre-bake. UHVCVD technique is suitable for manufacturing owing to its high throughput multiple-wafer growth process. The early work of GeSi UHVCVD epitaxy focused on high silicon content GeSi alloy films driven by the demands for mobility enhancement by strained GeSi in CMOS transistors (Meyerson, 1990). There are numerous work on this type of GeSi epitaxy, however it is not our primary interest in the photonic applications described in this chapter. There was some UHVCVD germanium epitaxy reports in the early 1990s (Kobayashi et al., 1990), while the extensive development of pure germanium epitaxy by UHVCVD began in the early to late 1990s (Currie et al., 1998; Luan et al., 1999) as a result of the booming photonics research.

On the other hand, germanium can also be grown with very high carrier (mainly hydrogen gas) flow rate at relaxed chamber base pressure. Rapid growth rate and surface passivation as a result of high carrier flow rate reduces of the chance of impurities contamination. The base pressure during growth e.g. tens of Torrs, is much higher than that in the UHVCVD case while lower than atmospheric pressure thereby this approach is called reduced pressure

chemical vapor deposition (RPCVD). Epitaxial germanium film with comparable threading dislocation density has been successfully grown on silicon using this approach (Hartmann et al., 2004). This approach quickly became popular as the maturely developed epitaxy reactors for (high silicon content) SiGe growth can be directly used with modified processes. It's also an approach compatible with manufacturing owing to its mature technique and rapid growth rate.

Besides the widely used UHVCVD and RPCVD approaches, there are a few other ways to grow germanium and high germanium content GeSi epitaxial films on silicon. Similarly to graded GeSi layers, GeSn can also be used as a buffer layer for germanium growth (Fang et al., 2007) though the research of the GeSn material system is still at its early stage. Epitaxial germanium has also been grown on silicon using a newly developed low energy plasma enhance chemical vapor deposition (LEPECVD) approach with low dislocation density (Osmond et al., 2009). The lack of germanium growth selectivity (between on silicon and on dielectrics) of this approach limits its use in many types of photonic devices. Besides direct epitaxy on silicon, an alternative way to form crystalline germanium on dielectrics through a so-called rapid melt growth (RMG) was introduced (Liu, Deal & Plummer, 2004). In this approach, amorphous germanium is deposited on top of dielectrics with a small window to expose crystalline silicon below the dielectrics. The germanium film is then capped with oxides and melt for a short time by rapid thermal annealing (RTA). Single crystalline germanium can be grown from the exposed silicon seed window through liquid-phase epitaxy (LPE) process. The RTA temperature profile is critical to the success of this approach though good quality of germanium film can be achieved.

As stated previously, the biggest challenge to grow high quality epitaxial germanium films with sufficient thickness is the lattice constant mismatch between germanium and silicon. To solve this problem a few approaches have been developed. A straightforward solution is to grow a graded GeSi layer or layers with the composition gradually changed from silicon to germanium. This approach was at first attempted in MBE growth (Fitzgerald et al., 1991) and was later introduced to UHVCVD growth (Samavedam & Fitzgerald, 1997) and RPCVD. It has been demonstrated that with a sufficiently thick graded layer high quality and low dislocated germanium films can be successfully grown on silicon (Currie et al., 1998).

A thick graded GeSi layer complicates epitaxial growth and device fabrication, so an alternative approach which uses a low temperature germanium layer (called buffer layer or seed layer) was developed (Colace et al., 1997). The low temperature buffer layer is used to kinetically prevent germanium from islanding and to plastically release lattice strain energy with misfit dislocations at Ge/Si interface when germanium thickness is beyond Stranski-Krastanov (S-K) critical thickness. In addition, another benefit of using low temperature is to make growing surface hydrogen act as surfactant to reduce island nucleation (Eaglesham et al., 1993). A thicker germanium film is then homo-epitaxially grown on the relaxed Ge buffer at higher temperatures for better growth rate. Therefore this approach is sometimes called two-step growth. The quality of germanium films by this type of growth is generally worse than the graded GeSi layer case, while the dislocations in the epitaxial film can be greatly minimized by a proper post annealing process (Luan et al., 1999).

Graded GeSi layer and low temperature Ge layer can both be used as buffer layer in germanium epitaxy and the required thickness of graded GeSi layer can be greatly reduced. Overgrowing germanium on a patterned silicon/SiO<sub>2</sub> surface is another way to reduce dislocations resulted from Ge/Si lattice mismatch (Langdo et al., 2000). The "epitaxial necking" process as a result of selective germanium growth on silicon and SiO<sub>2</sub> terminates



dislocations on SiO<sub>2</sub> sidewalls and leave the overgrown germanium above Si/SiO<sub>2</sub> layer with reduced dislocation densities. The disadvantage of this approach is the difficulty of surface morphology control and the inconvenience of using the fine patterned Si/SiO<sub>2</sub> surface in many cases.

### 1.3 Germanium band structure

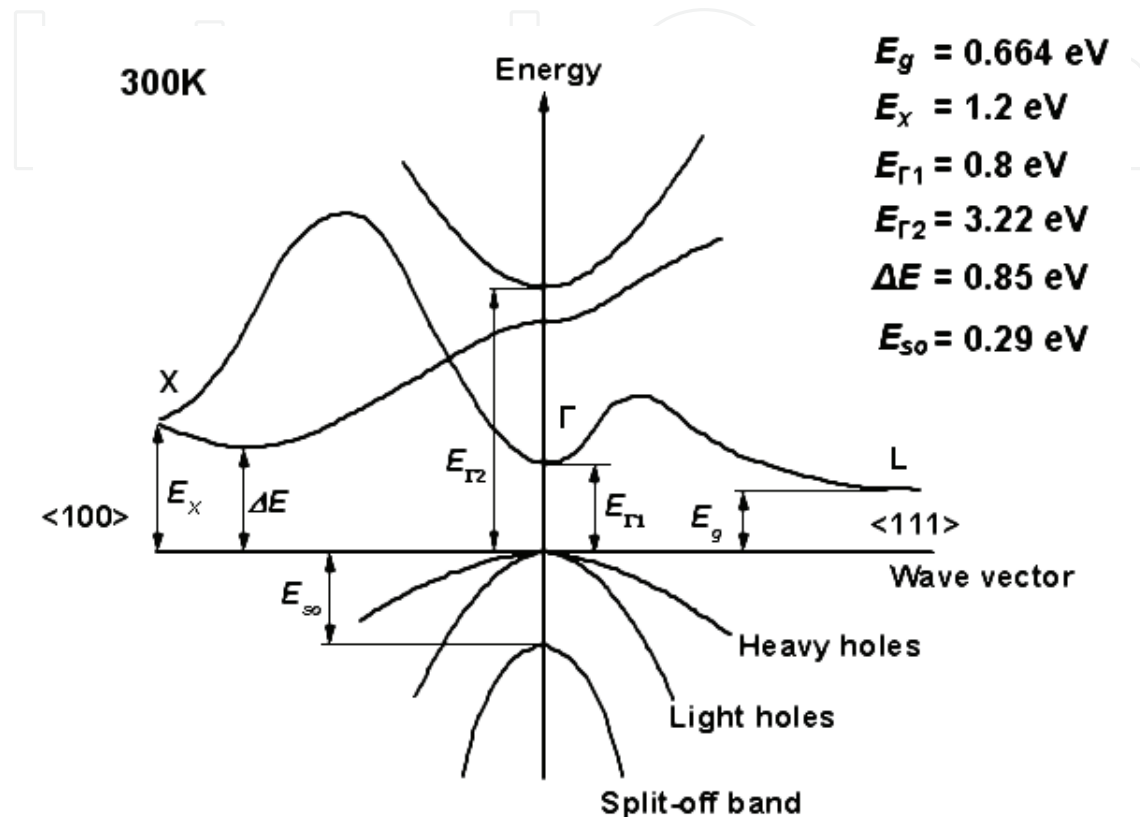


Fig. 1. Ge band structure at 300K.(M.Levinstein et al., 1996)

The electronic band structure of bulk germanium at room temperature is shown in Fig. 1. The valence band is composed of a light-hole band, a heavy-hole band, and a split-off band from spin-orbit interaction. The light-hole band and the heavy-hole band are degenerate at wave vector  $\mathbf{k} = 0$  or  $\Gamma$  point which is at the maximal energy of the valence band. The minimal energy of the conduction band is located at  $\mathbf{k} = \langle 111 \rangle$  or  $L$  point. The energy difference between the conduction band at  $L$  point and the valence band at  $\Gamma$  point determines the narrowest band gap in germanium:  $E_g = 0.664 \text{ eV}$ . This type of band gap is called an indirect band gap since the referred energies do not occur at the same  $\mathbf{k}$ . On the other hand, the two energy gaps between the two local minima of the two conduction bands and the maximum of the valence band at the same  $\Gamma$  point, i.e.  $E_{\Gamma 1}$  and  $E_{\Gamma 2}$  in Fig. 1, are called direct band gaps. Because the energy gap  $E_{\Gamma 2}$  is much larger than  $E_{\Gamma 1}$  and  $E_g$ , there is barely any electrons at such high energy levels so that it has negligible effect on the light-matter interaction in most cases. Therefore, people usually refer the direct band gap to  $E_{\Gamma 1}$  thus the author denotes  $E_{g\Gamma} \equiv E_{\Gamma 1}$  and  $E_{gL} \equiv E_g$  in the chapter. The part of the conduction band near  $\Gamma$  point is usually called direct valley or  $\Gamma$  valley while the part near  $L$  point is called indirect valley or  $L$  valley. In germanium crystal, the energy is 4-fold degenerate with regard

to the changes of the secondary total angular-momentum quantum number at  $L$  point, four  $L$  valleys are considered in the following calculations.<sup>1</sup>

#### 1.4 Germanium optical absorption

In the study of germanium in optoelectronic and photonic applications, one of the most important properties is the optical absorption. The band-to-band optical absorption is a process that transferring the energy of an incoming photon to an electron in valence band and make the electron jump to conduction band and leave a hole in valence band. When this process occurs in a crystalline material, both energy and momentum are conserved for the system. Therefore, the rate of such event is much lower in an indirect band-to-band transition compared to a direct band-to-band transition due to the need of one or more phonons to conserve momentum. The band structure described earlier indicates that the optical absorption of bulk germanium is substantial at any wavelengths less than  $1.55 \mu m$  (corresponding to  $0.80 eV$  direct band gap energy) and the direct optical absorption is what matters in most of the applications studied here.

The direct gap absorption of a semiconductor can theoretically modeled by solving the electron-photon scattering in crystalline potential with Fermi's golden rule. The detailed mathematical derivation is skipped the only the result is shown here:

$$\alpha(h\nu) = \frac{e^2 \hbar c \mu_0}{2m_e^2} \frac{|p_{cv}|}{n} \frac{1}{h\nu} \rho_r(h\nu - E_g), \quad (1)$$

where  $|p_{cv}|$  is related to an element of optical transition operator matrix and  $n$  is index of refraction, both of which are material properties and may be considered as constants within a small range of wavelengths.  $h\nu$  and  $E_g$  are the energy of photon and band gap respectively.  $\rho_r$  is the joint density of states of the conduction band ( $\Gamma$ valley) and the valence band. A quadratic approximation is usually adapted to describe the density of states near an extremum of any energy band in semiconductor and  $\rho_r$  is subsequently calculated

$$\rho_r(h\nu - E_g) = 2\pi \left( \frac{2m_r}{\hbar^2} \right)^{3/2} \sqrt{h\nu - E_g}, \quad (2)$$

where  $m_r = m_c m_v / (m_c + m_v)$  is the reduced effective mass as an expression of the effective masses of conduction band ( $m_c$ ) and the valence band ( $m_v$ ).

In a concise form, the direct gap absorption can be approximately written as

$$\alpha(h\nu) = A \frac{\sqrt{h\nu - E_g}}{h\nu}, \quad (3)$$

where  $A$  is a constant usually determined from experiments.

Some experimental optical absorption data of intrinsic and unstrained germanium at photon energies around its direct band gap (Braunstein et al., 1958; Dash & Newman, 1955; Frova & Handler, 1965; Hobden, 1962) are shown in Fig. 2. The sharp absorption drop at a photon energy of  $0.8 eV$  from all the data sources indicates the energy of the direct gap. The data from (Dash & Newman, 1955) and (Hobden, 1962) show good agreement at photon energies more

<sup>1</sup> Degeneracy with regard to the changes of electron spin quantum number is not explicitly accounted here though it is considered in density of states calculations.

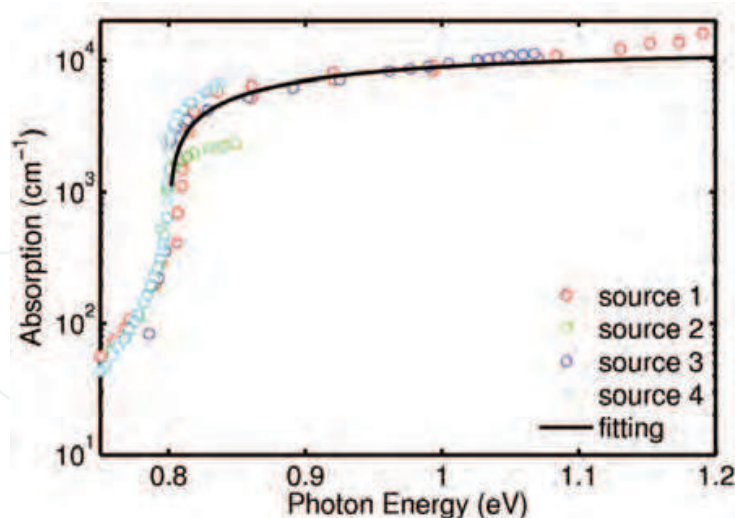


Fig. 2. Comparison of germanium absorption from different published sources. The experimental data (Source 1 to 4 in the figure) are obtained from (Braunstein et al., 1958; Dash & Newman, 1955; Frova & Handler, 1965; Hobden, 1962), respectively. The fitting based on the theoretical model is drawn with a black solid line.

than the direct gap. A calculation based on the above theoretical model (Equation 3) with  $A = 2.0 \times 10^4 \text{ eV}^{1/2}/\text{cm}$  is shown with black solid line and fits well with the experimental data.

## 2. Waveguide integrated germanium photodetector

### 2.1 Tensile strain engineering of germanium

For an integrated optical interconnect and transmission system on silicon platform, any wavelength above silicon absorption edge (about  $1.1 \mu\text{m}$ ) can be adopted for photon carriers as silicon is the guiding material. Shorter wavelengths can also be used if other compatible materials (e.g. silicon nitride) are used for wave guiding however silicon is a preferred material for the miniaturization reason owing to the high refractive index contrast between silicon and cladding materials (e.g. silicon oxide). But wavelengths near  $1.55 \mu\text{m}$  (fiber optics C-band) are commonly used because the communication design tool boxes at this wavelength band are mature in fiber optics technology. But germanium has weak absorption at  $1.55 \mu\text{m}$  which is about its direct band gap energy as described in the band diagram earlier. Germanium strain engineering has been adopted to address this issue.

Semiconductor band structure is associated with the crystal structure which can be altered by the existence of strain. This effect can be calculated using a strain-modified  $k \cdot p$  method Chuang (1995). Pikus-Bir Hamiltonian and Luttinger-Kohn's model are used in the method to describe the degenerate bands in germanium. This calculation shows that strain changes the energy levels of the direct  $\Gamma$  valley, the indirect  $L$  valleys, the light-hole band, and the heavy-hole band relative to vacuum level.<sup>2</sup> As a result, the direct band gap and indirect band gap are changed and the light-hole and the heavy-hole bands become non-degenerate with separation at  $\Gamma$  point. A band structure comparison of unstrained germanium and 0.2% tensile-strained germanium is shown in Fig. 3.

<sup>2</sup> The energy levels of other bands such as spin-orbit split-off band are also changed.



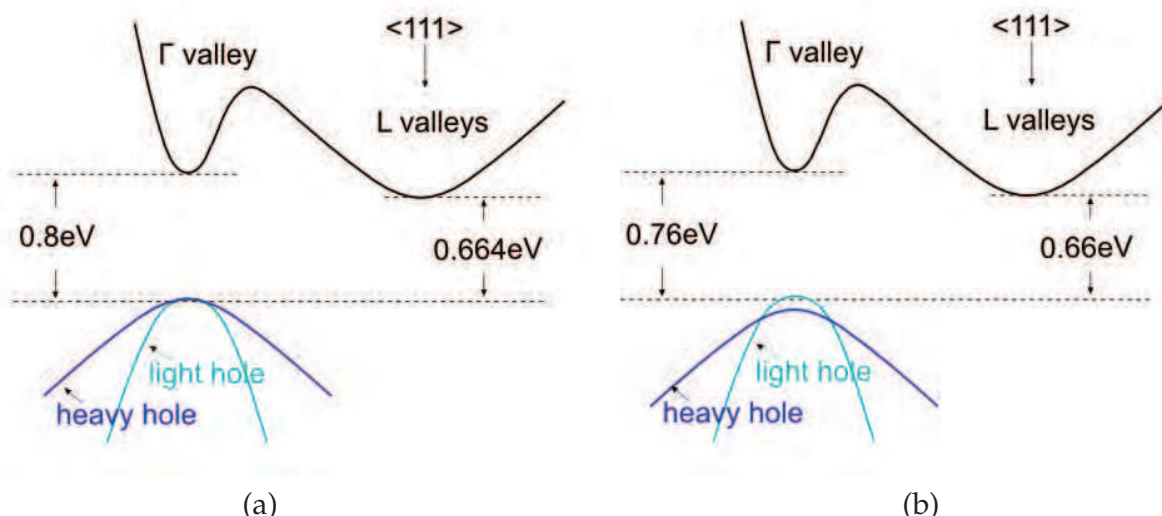


Fig. 3. Comparison of the band structures of (a) unstrained germanium and (b) strained germanium.

The direct band gap and indirect band gap under strain can be calculated using this method<sup>3</sup>

$$E_{g\Gamma hh} = a_{c\Gamma}(\epsilon_{xx} + \epsilon_{yy} + \epsilon_{zz}) + P + Q \quad (4)$$

$$E_{g\Gamma lh} = a_{c\Gamma}(\epsilon_{xx} + \epsilon_{yy} + \epsilon_{zz}) + P - Q/2 + E_{so}/2 - \sqrt{E_{so}^2 + 2E_{so}Q + 9Q^2} \quad (5)$$

$$E_{gLhh} = a_{cL}(\epsilon_{xx} + \epsilon_{yy} + \epsilon_{zz}) + P + Q \quad (6)$$

$$E_{gLlh} = a_{cL}(\epsilon_{xx} + \epsilon_{yy} + \epsilon_{zz}) + P - Q/2 + E_{so}/2 - \sqrt{E_{so}^2 + 2E_{so}Q + 9Q^2} \quad (7)$$

where

$$P = -a_v(\epsilon_{xx} + \epsilon_{yy} + \epsilon_{zz}) \quad (8)$$

$$Q = -b(\epsilon_{xx}/2 + \epsilon_{yy}/2 - \epsilon_{zz}) \quad (9)$$

.  $E_{g\Gamma hh}$  and  $E_{g\Gamma lh}$  are energy gaps between the  $\Gamma$  valley and the heavy-hole band and the light-hole band respectively.  $E_{gLhh}$  and  $E_{gLlh}$  are energy gaps between the  $L$  valley and the heavy-hole band and the light-hole band respectively.  $\epsilon_{xx}$ ,  $\epsilon_{yy}$ , and  $\epsilon_{zz}$  are strain components.  $E_{so}$  is the energy difference between valence bands and spin-orbit split-off band at  $\Gamma$  point.  $a_{c\Gamma}$ ,  $a_{cL}$ ,  $a_v$  and  $b$  are deformation potentials for  $\Gamma$  valley,  $L$  valleys, the average of three valence bands (light-hole, heavy-hole and spin-orbit split-off) and a strain of tetragonal symmetry. They are material properties which can be either calculated from first-principle calculation or determined by experiments.

For epitaxial germanium films, the strain is usually induced by in-plane stress from adjacent layers. If a biaxial stress is applied, i.e.

$$\epsilon_{xx} = \epsilon_{yy}, \quad (10)$$

the relation of the stress tensors for the isotropic material can be determined from Hooke's law in tensor form:

$$\epsilon_{zz} = -2C_{12}/C_{11}\epsilon_{xx}, \quad (11)$$

<sup>3</sup> Shear strain  $\epsilon_{xy}(x \neq y)$ , which is negligible in the thin film material, is not considered here.

where  $C_{11}$  and  $C_{12}$  are the elements of the elastic stiffness tensor.

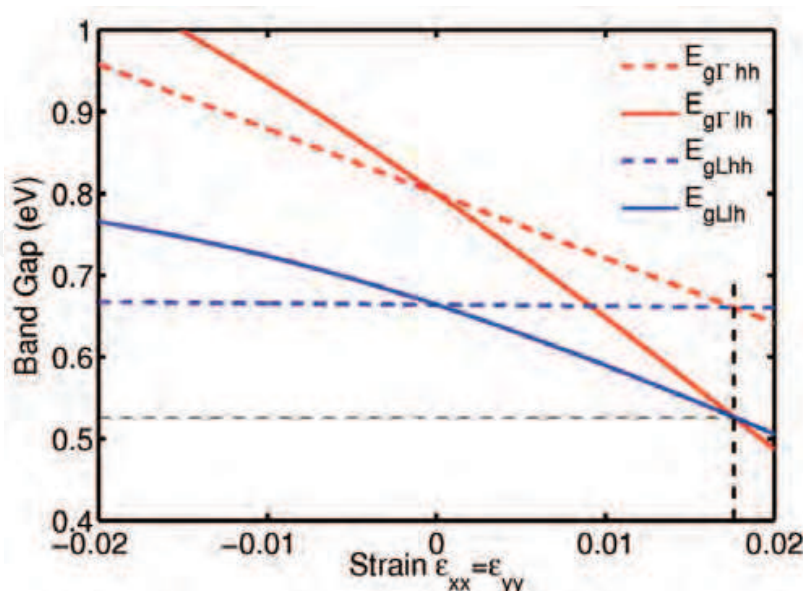


Fig. 4. The direct and the indirect band gaps of germanium with in-plane strain.  $E_{g\Gamma hh}$  and  $E_{g\Gamma lh}$  are energy gaps between the  $\Gamma$  valley and the heavy-hole band and the light-hole band respectively.  $E_{gLhh}$  and  $E_{gLlh}$  are energy gaps between the  $L$  valley and the heavy-hole band and the light-hole band respectively.

The direct and the indirect band gaps of strained germanium can be obtained using Eq. 4–7 with the experimental results of  $a_{c\Gamma} = -8.97$  eV and  $b = -1.88$  eV from reference (Liu, Cannon, Ishikawa, Wada, Danielson, Jongthammanurak, Michel & Kimerling, 2004)  $C_{11} = 128.53$  GPa and  $C_{12} = 48.26$  GPa from reference (Madelung & et al, 1982), and the calculated results of  $a_{cL} = -2.78$  eV and  $a_v = 1.24$  eV from reference (de Walle, 1989). These energy gaps are calculated and shown in Fig. 4. We can see both the direct band gap and the indirect band gap shrink with tensile strain (positive  $\epsilon_{xx}$ ) and the direct band gap decreases faster than the indirect band gap does due to  $|a_{c\Gamma}| > |a_{cL}|$ . The direct band gap becomes equal to the indirect band gap at  $\epsilon \approx 1.8\%$  where Ge becomes a direct band gap material. The energy gaps from the conduction band (equal for both direct  $\Gamma$  valley and indirect  $L$  valley) to the light-hole and the heavy-hole band are 0.53 eV and 0.66 eV respectively. It is noted that there are two kinds of energy gaps at both  $\Gamma$  point and  $L$  point due to the separation of the light-hole band and the heavy-hole band. The optical band gap is determined by the smaller gap with respect to the light-hole band. We refer the band gap to this energy gap in the following discussion unless explicitly stated otherwise.

The absorption edge of tensile strain germanium moves towards lower energy because of the shrinkage of the direct band gap. Since the light-hole band and the heavy-hole band separate under strain, two optical transitions corresponding to the two energy gaps contribute the overall optical absorption. Therefore the absorption spectrum of tensile-strain germanium can be expressed as

$$\alpha(h\nu) = A \left( k_1 \frac{\sqrt{h\nu - E_{g\Gamma lh}}}{h\nu} + k_2 \frac{\sqrt{h\nu - E_{g\Gamma hh}}}{h\nu} \right), \quad (12)$$

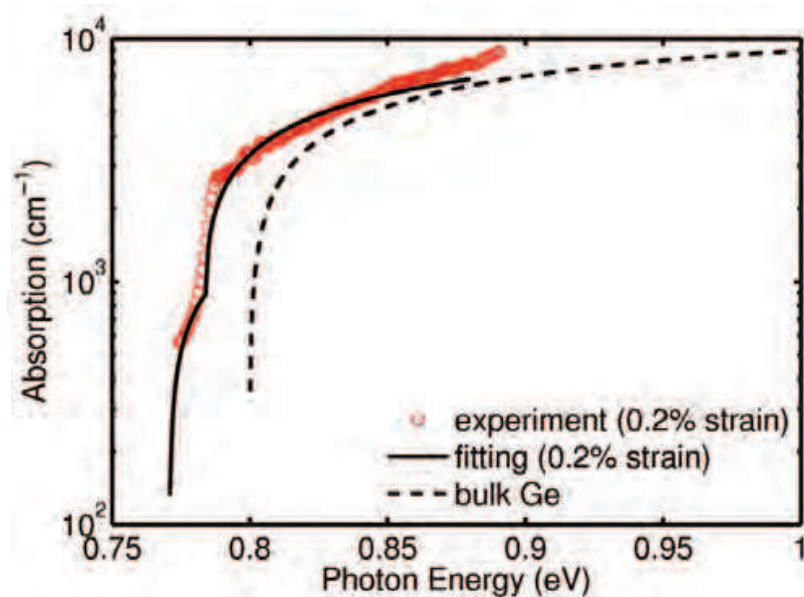


Fig. 5. The experimental result and the theoretical fitting of the optical absorption of 0.2% tensile-strained germanium. The optical absorption of unstrained germanium is shown with a black dash line for comparison.

where  $k_1 = m_{rlh}^{3/2} / (m_{rlh}^{3/2} + m_{rhh}^{3/2})$  and  $k_2 = m_{rhh}^{3/2} / (m_{rlh}^{3/2} + m_{rhh}^{3/2})$  are coefficients attributing to the difference between the two transitions due to the different reduced effective masses.  $k_1$  and  $k_2$  are normalized so that  $k_1 + k_2 = 1$ .  $k_1 = 0.68168$  and  $k_2 = 0.31832$  are calculated for germanium. The measured absorption spectrum of 0.2% tensile-strained germanium is shown in Fig. 5 and  $A = 1.9 \times 10^4 \text{ eV}^{1/2}/\text{cm}$  is calculated by fitting the experimental result using Eq. 12. The  $A$  of strained germanium is approximately the same as that of unstrained germanium which underlies that applied strain is too small to affect the optical transition matrix of Fermi's golden rule.

Introduction of tensile strain in germanium is not intuitive in germanium-on-silicon epitaxy. It is usually understood that strain is induced from the lattice mismatch between epitaxial and substrate materials. In such way, epitaxial germanium is compressively strained as the lattice constant of germanium (5.658 Å) is greater than that of silicon (5.431 Å). However, the above analysis is only applied to the case that an epitaxial layer is thinner than its critical thickness on a certain substrate. Beyond this thickness, the elastic strain of the epitaxial film releases plastically by introducing misfit dislocations near material interface region. Another possible result beyond critical thickness is that three dimensional growth (islanding) occurs to balance elastic strain energy with surface tension.

In the two-step growth described earlier, the buffer layer is grown at low temperature to prevent such islanding process by reducing the mobility of adsorbed atoms on growing surface. Thus the following germanium layer grown at higher temperatures layer is on a strain-relaxed surface of the buffer layer, the thickness which is more than critical thickness. The epitaxial germanium and the silicon substrate shrink as the substrate temperature is cooled down to room temperature. Germanium shrinks more due to its larger coefficient of thermal expansion than that of silicon therefore in-plane tensile strain is accumulated in the germanium film as illustrated in Fig. 6.

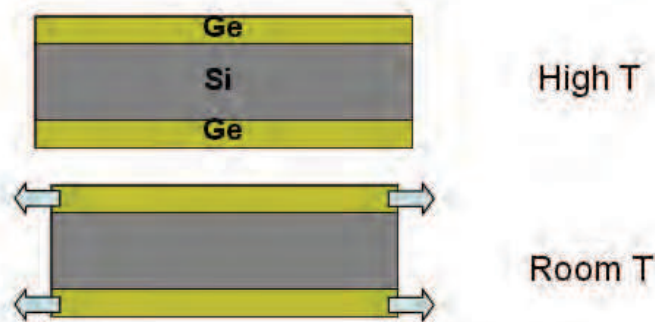


Fig. 6. Illustration of tensile strain formation in germanium on silicon epitaxy.

As silicon substrate is always much thicker than germanium epitaxial layer, the tensile strain  $\epsilon_{//}$  in germanium caused by in-plane stress can be obtained using

$$\epsilon_{//} = \int_{T_0}^{T_1} (\alpha_{\text{Ge}} - \alpha_{\text{Si}}) dT, \tag{13}$$

where,  $T_0$  and  $T_1$  are room temperature and growth temperature respectively, and  $\alpha_{\text{Ge}} = \alpha_{\text{Ge}}(T)$  and  $\alpha_{\text{Si}} = \alpha_{\text{Si}}(T)$  are thermal expansion coefficients of germanium and silicon respectively. In general, these coefficients are a function of temperature and the relations are experimentally determined (Singh, 1968) and (Okada & Tokumaru, 1984):

$$\alpha_{\text{Ge}}(T) = 6.050 \times 10^6 + 3.60 \times 10^9 T - 0.35 \times 10^{-12} T^2 (^{\circ}\text{C}^{-1}), \tag{14}$$

$$\alpha_{\text{Si}}(T) = 3.725 \times 10^{-6} \times [1 - \exp(-5.88 \times 10^{-3} \times (T + 149.15))] + 5.548 \times 10^{-10} T (^{\circ}\text{C}^{-1}). \tag{15}$$

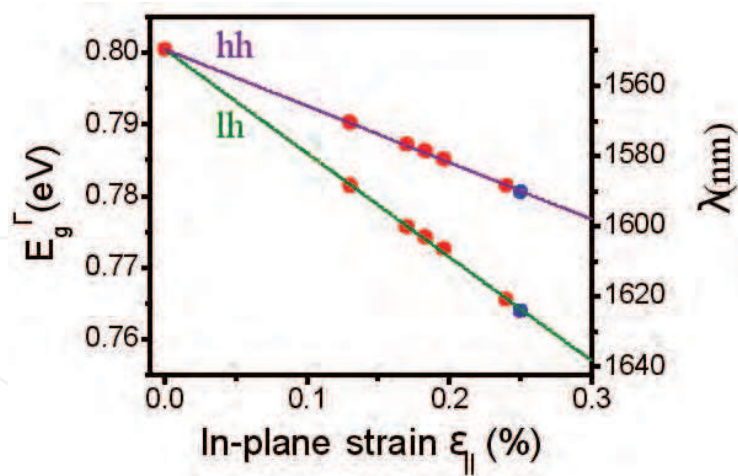


Fig. 7. Ge direct energy gaps versus tensile strain measured by X-ray diffraction (XRD) and photoreflectance (PR) experiments. (Liu, Cannon, Ishikawa, Wada, Danielson, Jongthammanurak, Michel & Kimerling, 2004)

From the above formula, different tensile strain can be achieved with different growth temperature and the experimental results of germanium grown at various temperatures are also plotted in Fig. 7. The energy gaps are measured by photoreflectance (PR) experiment and the tensile strain is obtained from crystal lattice constant measurement by X-ray diffraction



(XRD) (Liu, Cannon, Ishikawa, Wada, Danielson, Jongthammanurak, Michel & Kimerling, 2004). The direct-gap deformation potentials of germanium can then be calculated from fitting the experimental data. The calculated two direct energy gaps, i.e. from the direct  $\Gamma$  valley to the light-hole band (indicated by lh) and to the heavy-hole band (indicated by hh) respectively, of germanium as a function of tensile strain are shown in Fig. 7 with the fitted deformation potentials.

If post-growth thermal annealing is performed, germanium epitaxial layer is further relaxed at the annealing temperature therefore more tensile-strain is possibly obtained at room temperature. In practice, it is found that the tensile strain in germanium cease to increase at temperatures beyond about 750 °C and the measured strain is usually less than the theoretical values calculated from above formula (Cannon et al., 2004). It is believed that the existence of residual compressive strain retrains the full relaxation of germanium.

## 2.2 Germanium photodetector

Germanium has been investigated as an efficient photodetector on silicon platform since the germanium MBE was realized. Although the early work of germanium on silicon photodetector was in 1980s (Luryi et al., 1984), it only became extensively researched since late 1990s aligned with the boom of CVD epitaxy of germanium on silicon (Colace et al., 2000; 1998; Dehlinger et al., 2004; Hartmann et al., 2004; Liu, Michel, Giziewicz, Pan, Wada, Cannon, Jongthammanurak, Danielson, Kimerling, Chen, Ilday, Kartner & Yasaitis, 2005; Luan et al., 2001).

Early epitaxial germanium photodetectors are mostly vertical P-N or P-I-N junction devices designed for surface optical incidence for the ease of fabrication. There is a trade-off between optical absorption and carrier transit time for this type of photodetector and many of devices are designed for a 3dB bandwidth less or around 10GHz for 10 Gb/s applications (Colace et al., n.d.; Liu, Michel, Giziewicz, Pan, Wada, Cannon, Jongthammanurak, Danielson, Kimerling, Chen, Ilday, Kartner & Yasaitis, 2005; Morse et al., 2006). A lateral P-I-N junction design can be adopted to reduce carrier transit time for very high speed applications though the photo responsivity is usually compromised (Dehlinger et al., 2004). Therefore, waveguide coupled germanium photodetectors are favored in high speed applications especially for devices working at 1.55  $\mu\text{m}$  in which longer germanium absorption length is required due to weaker absorption.

The speed of photodetectors is characterized by its 3dB bandwidth which is usually limited by a combination of Resistive-capacitive (RC) delay and carrier transit time. The RC delay limited 3dB bandwidth is

$$f_{RC} = \frac{1}{2\pi RC}. \quad (16)$$

It can be proved that the carrier transit time limited 3dB bandwidth is

$$f_{tr} = 0.44 \times \frac{v_d}{d}, \quad (17)$$

where  $v_d$  is the average drift velocity of carriers (electrons or holes) and  $d$  is the junction depletion width in germanium.  $v_d$  is generally a function of electric field (and temperature) but it approaches the saturation velocity  $v_{sat}$  when applied electric field is sufficiently large. The experimentally measured electron drift velocity in germanium as a function of electric field (Jacoboni et al., 1981) is shown in Fig. 8. This relation can be described by an empirical



formula:

$$v_d = \frac{1}{(1/(v_{sat})^n + 1/(\mu E)^n)^{1/n}}, \tag{18}$$

where  $\mu = 3.7 \times 10^3 \text{ cm}^2/\text{V} \cdot \text{s}$  is the electron mobility and  $n = 2.5$  is a coefficient determined empirically. The saturation velocity of electrons in germanium is about  $6 \times 10^6 \text{ cm/s}$  while the value is a little less for holes.

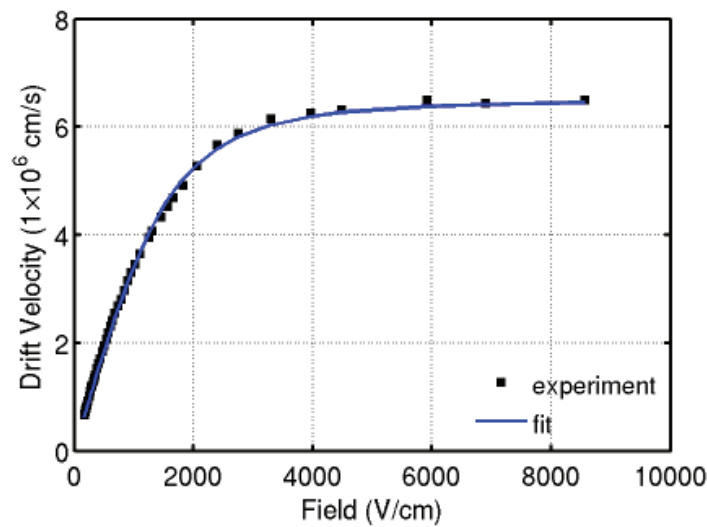


Fig. 8. Experimental result and theoretical fitting of the electron drift velocity in germanium versus electric field.

When both RC delay and transit time are considered the overall 3dB bandwidth is

$$f_{3dB} = \frac{1}{\sqrt{1/f_{RC}^2 + 1/f_{tr}^2}}. \tag{19}$$

Based on this formula, the calculated 3dB bandwidth contour of a germanium diode with respect to its depletion width and device area is shown in Fig. 9. In general, the transit time limits the maximal thickness of depletion width which is close to the germanium thickness for a fully depleted vertical P-I-N junction diode. The RC delay, on the other hand, limits the maximal device area. In the calculation, a termination resistance of 50 Ω is used for the compatibility of common impedance and no parasitics is considered. When the series resistance and parasitic capacitance (e.g. contact pad capacitance) are taken into account, the 3dB bandwidth is reduced.

Dark current is another important parameter of photodetectors. Germanium photodetector usually suffers from a larger dark current as a result of its narrow indirect band gap and poor surface passivation capability. A narrow band gap leads to higher density of intrinsic carriers and higher trap assisted generation rate through Shockley-Read-Hall (SRH) process. The surface passivation of germanium, i.e. termination of the dangling bonds or surface states, is generally more different than silicon as germanium oxide is much less robust than silicon dioxide. Therefore people use other materials such as hydrogenate amorphous silicon (aSi:H), hydrogen-rich silicon nitride (Si<sub>3</sub>N<sub>4</sub>), germanium oxynitride (Ge(ON)<sub>x</sub>) and etc. to passivate germanium surface. The dark current associated with material quality (e.g. defects)

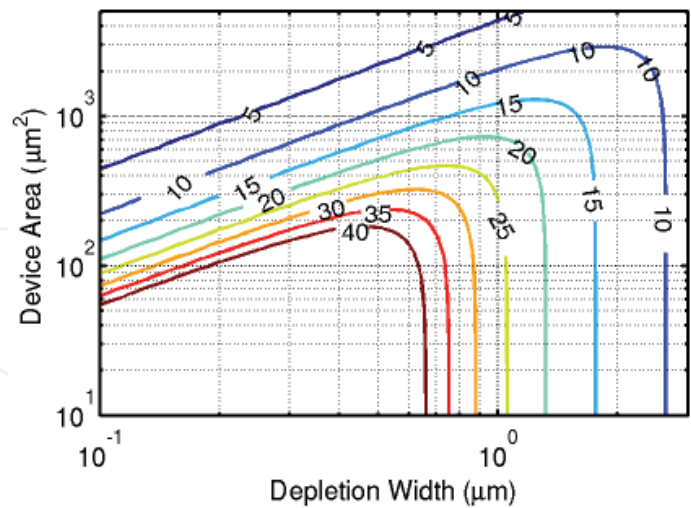


Fig. 9. Calculated 3dB bandwidth contour of a germanium diode with respect to its depletion width and device area in ideal conditions.

is sometimes called bulk leakage while that with surface condition is called surface leakage. The former one is scaled with the area of devices while the latter one is scaled with the perimeter.

As surface leakage highly depends on surface passivation processes, bulk leakage is a good measure of material quality. In many epitaxial germanium photodetectors with relatively larger size, bulk leakage dominates overall dark current. As we mentioned earlier in this chapter, misfit dislocations exist at germanium and silicon interface as a result of lattice mismatch and stress relaxation. These misfit dislocations along with other crystal imperfections are important sources of threading dislocations in germanium. These threading dislocations introduce deep level traps (SRH recombination-generation centers) which result in the majority of bulk leakage current in many cases. The effect of threading dislocation on leakage current can be obtained by calculating generation current induced by deep level traps:

$$J_{gen}/d = \frac{en_i}{\tau}, \tag{20}$$

where  $J_{gen}/d$  is the generation current per unit length,  $e$  is elementary charge,  $n_i$  is intrinsic carrier density and the minority lift time  $\tau$  is equal to

$$\tau = \frac{1}{\sigma v_{th} N_D N_{TD}}, \tag{21}$$

where  $\sigma$  is trap capture cross-section,  $v_{th}$  is carrier thermal velocity,  $N_D$  is threading dislocation density and  $N_{TD}$  is the number of traps per unit length of dislocation. By substituting the expression of  $\tau$  the current density per length

$$J_{gen}/d = en_i \sigma v_{th} N_D N_{TD}. \tag{22}$$

The above formula can be applied to either electrons or holes though one of them usually dominates the generation process. In germanium,  $v_{th} = 2.3 \times 10^7$  cm/s for electrons and  $v_{th} = 1.7 \times 10^7$  cm/s for holes. The trap capture cross section is different for different types of traps

and it usually between  $1 \times 10^{-14} \text{ cm}^{-2}$  to  $1 \times 10^{-15} \text{ cm}^{-2}$ . The leakage current density per unit length as a function of threading dislocation density is calculated by using  $\sigma = 1 \times 10^{-15} \text{ cm}^{-2}$  for  $N_{TD} = 1 \times 10^7 \text{ cm}^{-1}$  and  $N_{TD} = 1 \times 10^8 \text{ cm}^{-1}$ , respectively. The results are shown in Fig. 10. A few experimental results (Colace et al., n.d.; Fama et al., n.d.; Liu, Cannon, Wada, Ishikawa, Jongthammanurak, Danielson, Michel & Kimerling, 2005; Samavedam et al., 1998; Sutter et al., 1994) are also presented in the figure for comparison. For the experimental results, the dark current density is divided by the germanium thickness as an approximating for the depletion width. All the experimental results fall in the two calculation curves and show good agreement with the calculated relation.

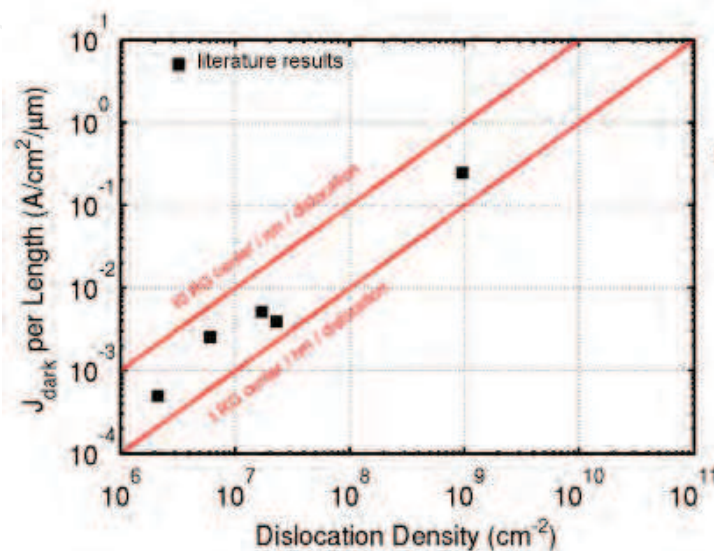


Fig. 10. Summary of dark current density (at -1V) bias versus measured threading dislocation density from various literature (Colace et al., n.d.; Fama et al., n.d.; Liu, Cannon, Wada, Ishikawa, Jongthammanurak, Danielson, Michel & Kimerling, 2005; Samavedam et al., 1998; Sutter et al., 1994). Theoretical calculation with two conditions of generation-recombination center per unit length are shown in two solid lines.

### 2.3 Integration of germanium photodetector and waveguide

Waveguide coupled photodetector is adopted to break the trade-off between optical absorption and device speed as stated earlier. It also allows the realization of planar integration of photodetectors with electronics on silicon substrate. Therefore many research work on silicon waveguide coupled germanium photodetectors emerged soon after the surge of surface incidence epitaxial germanium photodetector research. The research started with polycrystalline germanium on silicon waveguide (Colace et al., 2006) followed by numerous work of waveguide coupled epitaxial germanium photodetectors around the world. In most of these work, silicon-on-insulator is the choice for substrate to form silicon waveguide with optical confinement by buried oxide and surrounding low refractive index materials (Feng et al., 2009; 2010; Masini et al., 2007; Vivien et al., 2009; 2007; Wang, Loh, Chua, Zang, Xiong, Loh, Yu, Lee, Lo & Kwong, 2008; Wang, Loh, Chua, Zang, Xiong, Tan, Yu, Lee, Lo & Kwong, 2008; Yin et al., 2007) while silicon nitride can also be adopted as waveguide to couple light into germanium (Ahn et al., 2007). Most of these photodetectors are vertical or lateral P-I-N diodes while quantum well germanium photodetectors are also investigated (Fidaner

et al., 2007). Among these devices, more than 30GHz 3dB bandwidth have been achieved at reasonable bias (usually -1V to -2V) with good responsivity (e.g. 0.9-1.0 A/W). These high speed photodetectors can be potential substitutes for commercially available photodetectors based on III-V materials for up to 25Gb/s digital transmission applications.

In waveguide coupled photodetectors, one of the critical design roles is to optimize waveguide to germanium optical coupling. The required length of a photodetector is determined by the coupling efficiency for an evanescent coupling. Therefore the device speed is also affected by coupling design as the capacitance of the device is scaled with its dimension. In general, the germanium is on top of an input silicon waveguide for evanescent coupling. This design is usually adopted for small silicon waveguides such as channel waveguides or small rib waveguides on SOI substrates with relatively thin device silicon layer. However, for a large rib waveguide the coupling efficiency is very sensitive to the thickness of germanium layer as shown later. Therefore it is sometimes necessary to make a mode converter to push guided light down to the slab part of the rib waveguide and couple the light from the slab to germanium photodetectors. The two different designs are schematically shown in Fig. 11.

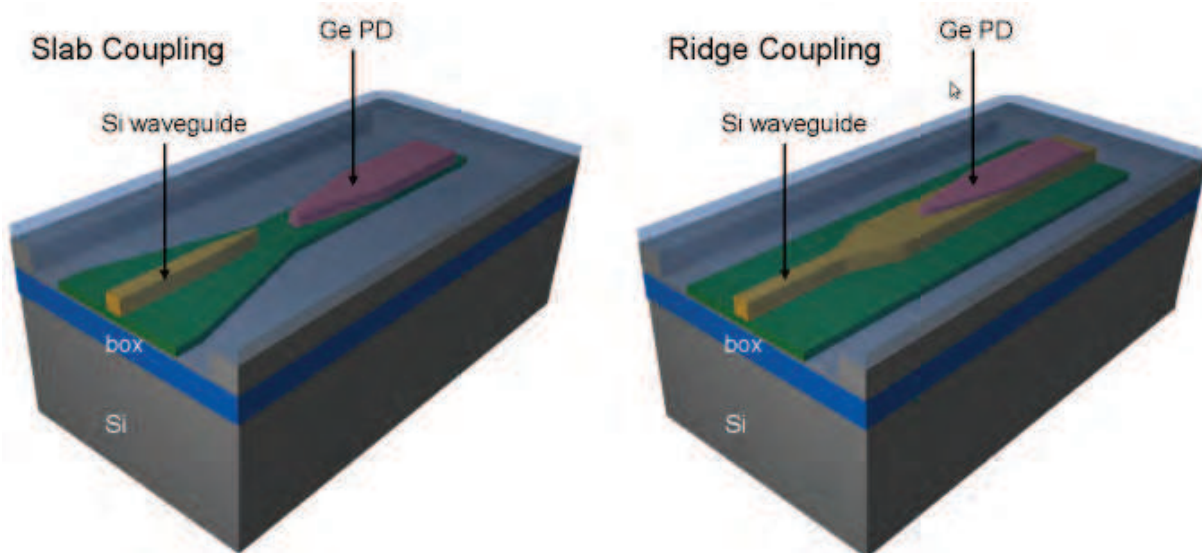


Fig. 11. Two designs of waveguide to germanium photodetector coupling on SOI substrate.

The coupling between waveguide and germanium can be simulated by numerical methods such as finite-difference time-domain (FDTD) method. A sample simulation results is shown in Fig. 12. In the figure, the propagated electric field shows the process of evanescent coupling. By calculating the absorption in germanium in this coupling process, the ideal responsivity can be obtained. Simulated ideal responsivity as a function of germanium thickness for waveguide-coupled photodetector with two silicon thicknesses ( $0.55\mu\text{m}$  and  $0.8\mu\text{m}$ ) are shown in Fig. 13. The responsivity is generally a periodic function of germanium thickness as a result of coupling resonance conditions. But the sensitivity of peak responsivity on germanium thickness is higher for thicker silicon thickness. It is the reason of reducing silicon thickness for large silicon rib waveguides to avoid the sensitivity of the performance of germanium photodetectors due to processing variations. The reduction of the coupling sensitivity on the polarization state of guided modes is another design consideration. The peak coupling conditions of a transverse-electric (TE) mode and a transverse-magnetic (TM) mode are not usually aligned. Optimizing TE and TM modes or creating multiple modes in the waveguides with some mode transformers can minimize the polarization sensitivity.



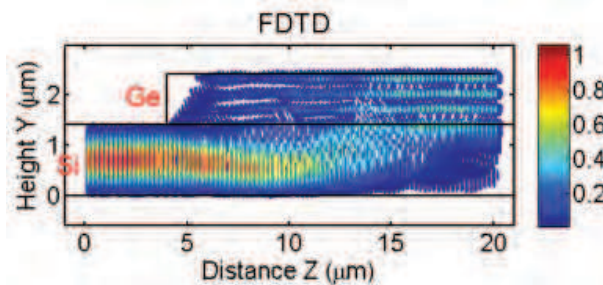


Fig. 12. FDTD simulation of light coupling from silicon waveguide to germanium photodetector.

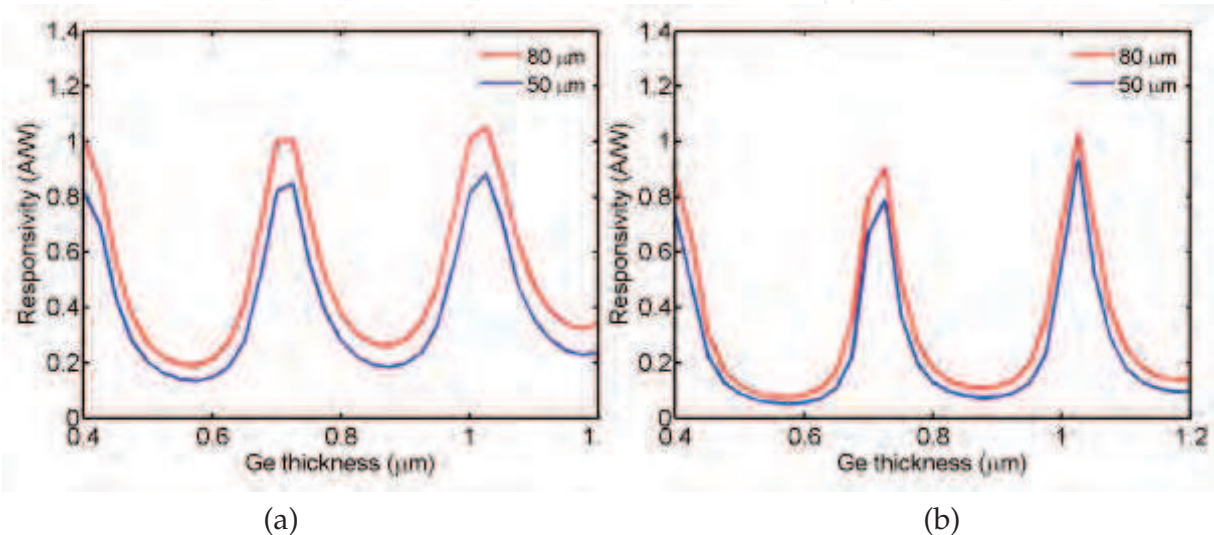


Fig. 13. Simulated ideal responsivity versus germanium thickness for waveguide-coupled photodetector with silicon thickness of (a)  $0.55\mu\text{m}$  and (b)  $0.8\mu\text{m}$ , respectively.

### 3. Germanium light source

#### 3.1 Silicon based light source

Photonic-electronic monolithic integration requires a silicon-based light source. A silicon-based laser is arguably the most challenging element in silicon photonics because both silicon and SiGe (including pure germanium) are inefficient light emitters due to their indirect band structure. Many approaches have been investigated to solve this challenge including the efforts on porous silicon (Gelloz & Koshida, 2000; Koshida & Koyama, 1992), silicon nanostructures (Irrera et al., 2003) and SiGe nanostructures (Peng et al., 1998), silicide (Leong et al., 1997), erbium doped silicon (Zhang et al., 1994). However, all above approaches are challenged by the lack of sufficient gain to surpass material loss for laser action.

Erbium-doped silicon dielectrics which benefit from less energy back transfer than erbium-doped silicon are potential gain media. Erbium atoms which are capable of light emission at  $1.54\mu\text{m}$  have been incorporated into silicon oxide (Adeola et al., 2006; Fujii et al., 1997; Kik et al., 2000) or silicon nitride (Makarova et al., 2008; Negro et al., 2008) matrix materials. Silicon nanocrystals are sometimes introduced in these materials as recombination sensitizers. The optical gain of such extrinsic light-emitting materials is generally very small (Han et al., 2001) due to limited erbium solubility and energy up-conversion. Therefore lasing can only occur in extremely low loss resonators such as toroidal structures (Polman



et al., 2004). These dielectric materials also suffer from the difficulty of electrical injection. Appreciable concentration of carriers only presents under very high electric field via effects like tunneling process (Iacona et al., 2002; Nazarov et al., 2005).

Non-linear optical effects can also produce net gain in silicon. Based on stimulated Raman scattering (SRS) effect, optically pumped silicon waveguide lasers have been realized with pulse (Boyras & Jalali, 2004; Rong et al., 2004) and continuous-wave operation (Rong et al., 2005). Similarly, the inevitable requirement of optical injection makes them not suitable for integrated photonics.

Following a hybrid approach, researchers successfully integrated III-V semiconductor lasers on silicon substrates. The integration can be accomplished by directly growing GaAs/InGaAs on silicon with graded  $\text{Si}_x\text{Ge}_{1-x}$  buffer layers (Groenert et al., 2003) or bonding III-V materials on silicon surface for laser fabrication (Fang et al., 2006; Park et al., 2005).

Electronic-photonic monolithic integration requires a light source with the capability of electrical injection and room temperature operation based on silicon compatible materials and CMOS-compatible processes. Germanium is a very promising material for making such a light source if it can be engineered for more efficient direct gap light emission and net optical gain.

### 3.2 Germanium band structure engineering

The inefficiency of light emission from germanium comes from its indirect band structure. To understand how we can engineer its band structure for more efficient light emission and even net optical gain we start with the carrier recombination analysis in germanium.

The band structure and the carrier distribution of germanium at equilibrium are drawn in the Fig. 14 (a). Most of the thermally activated electrons occupy the lowest energy states in the indirect  $L$  valleys governed by Fermi distribution:

$$f(E) = \frac{1}{1 + (E - E_f)/k_B T}, \quad (23)$$

where  $E_f$  is equilibrium Fermi level. For a direct gap material InGaAs shown in Fig. 14 (b), most of the electrons occupy the direct  $\Gamma$  valley.

The carrier occupancy states determine the light emitting properties of a material. The band-to-band optical transition requires excess free carriers which are injected electrically or optically. At steady state, the carriers obey quasi Fermi distribution with respect to carrier quasi Fermi level:

$$f_c(E) = \frac{1}{1 + (E - E_{fc})/k_B T}, \text{ and} \quad (24)$$

$$f_v(E) = \frac{1}{1 + (E - E_{fv})/k_B T}, \quad (25)$$

where  $E_{fc}$  and  $E_{fv}$  are the quasi Fermi levels of electrons and holes. A single quasi Fermi level exists for electrons or holes in steady state despite of the multi-valley band structure because of very fast inter-valley scattering process.

The carrier distribution under injection for germanium and InGaAs are shown in Fig. 15. Despite germanium is an indirect band gap material, there are still some electrons pumped to the  $\Gamma$  valley owing to the small energy difference (0.136 eV) between the direct band gap and the indirect band gap. The excess electrons in the  $\Gamma$  valley recombine radiatively with the holes in the valence band. This light emission process is as efficient as the direct

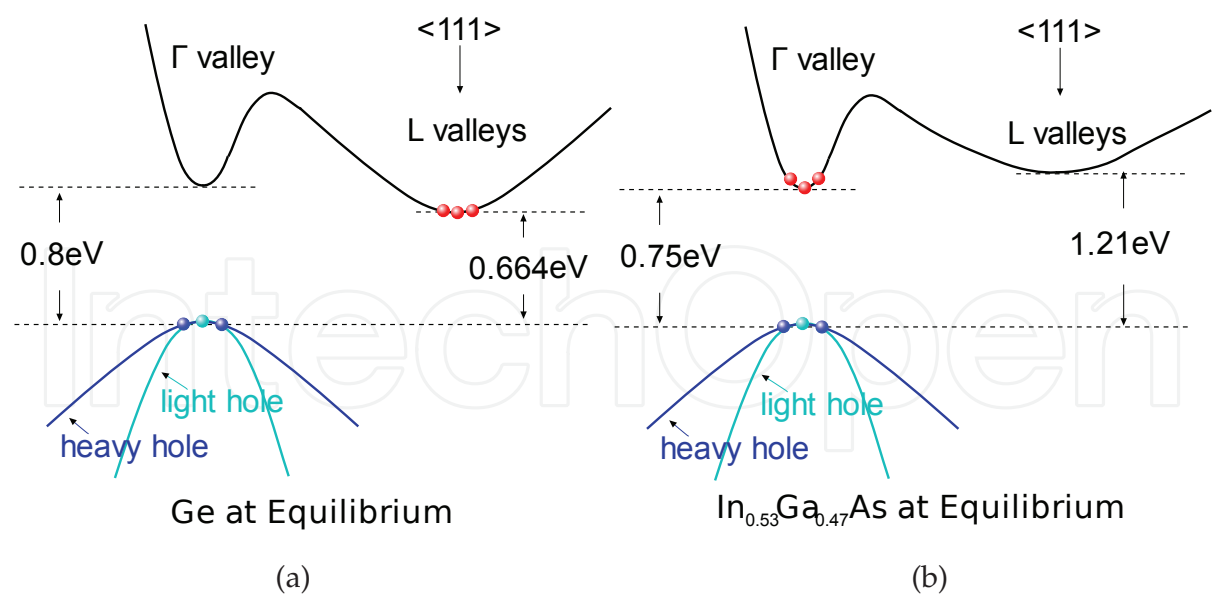


Fig. 14. Comparison of the band structure and the carrier distribution between (a) Ge and (b) In<sub>0.53</sub>Ga<sub>0.47</sub>As at equilibrium.

radiative recombination in direct band gap materials. But the overall light emission from germanium is weak because most of the injected electrons are in the  $L$  valleys. Most of these electrons recombine non-radiatively as indirect phonon-assisted radiative recombination is very slow. For III-V direct gap materials, injected electrons are in the direct valley so overall light emission is efficient.

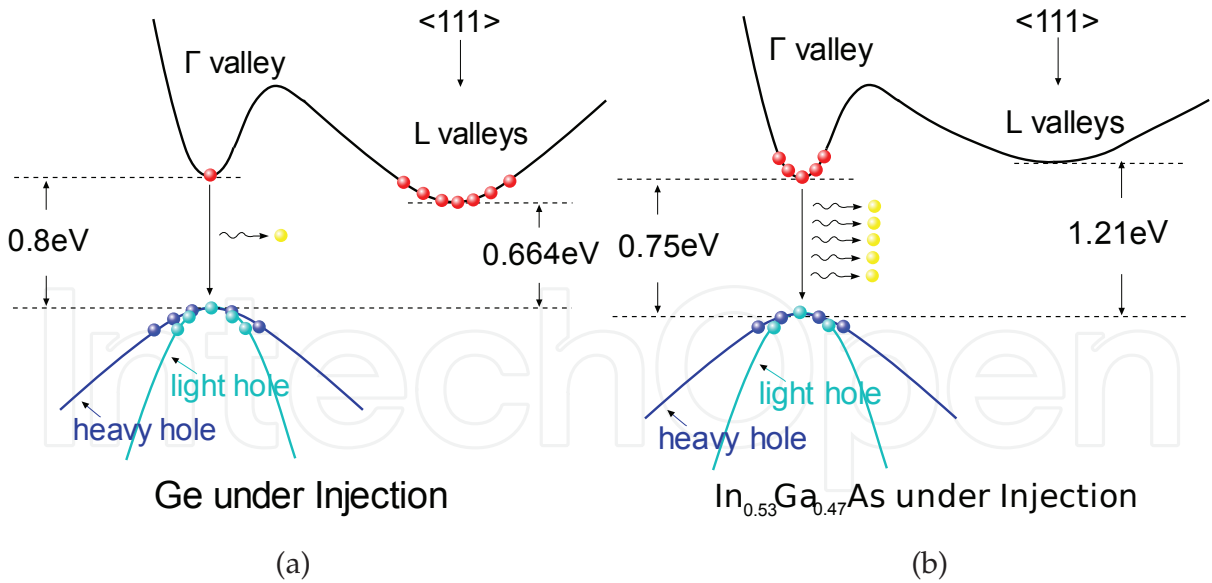


Fig. 15. Comparison of the carrier distribution and the light emission process between (a) Ge and (b) In<sub>0.53</sub>Ga<sub>0.47</sub>As under injection.

To improve the light emission efficiency in germanium, more injected electrons are required to be pumped into  $\Gamma$  valley. In other words, the objective is to make germanium a direct gap material. In the germanium photodetector section, it has shown that tensile strain can be used to reduce direct band gap for more optical absorption. It should also be noted that the difference

of direct and indirect band gaps are also reduced under tensile strain. Based on the calculation a tensile strain of about 1.8% is required to make germanium direct band gap. It is difficult to achieve such high strain in epitaxial germanium. By using a thermal mismatch approach to stress epitaxial germanium on silicon as explained earlier, the maximal tensile strain is below 0.20~0.25%. The energy difference between the direct and the indirect gaps at this condition is only reduced by 20 meV therefore the majority of the injected electrons still occupy the indirect  $L$  valleys.

N-type doping can be used to solve this problem. When the indirect  $L$  valleys are filled with the extrinsic electrons thermally activated from n-type donors, the Fermi level is raised to push more injected electrons into the direct  $\Gamma$  valley. An example of the Fermi level versus active n-type doping concentration for 0.25% tensile-strained germanium is shown in Fig. 16. The Fermi level becomes equal to the bottom of  $\Gamma$  valley at a doping concentration of  $7 \times 10^{19} \text{ cm}^{-3}$ , where most states of the indirect  $L$  valleys are filled by electrons and Ge behaves as a direct band gap material.

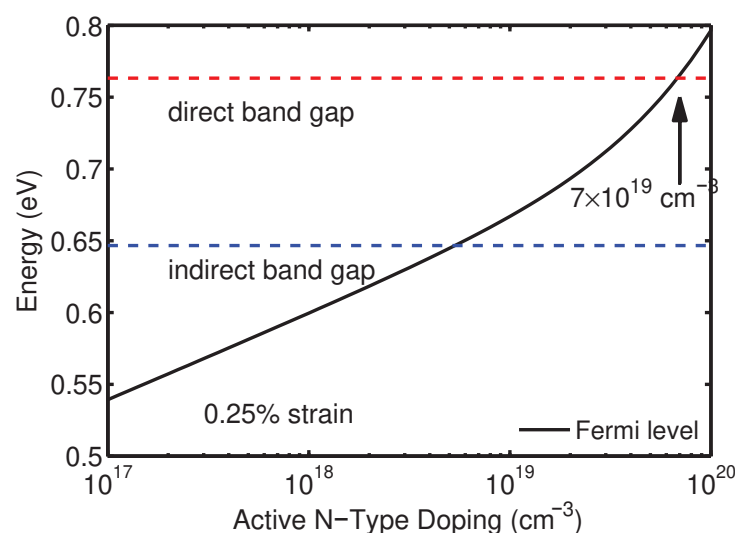


Fig. 16. Calculations of the Fermi level as a function of active n-type doping concentration in 0.25% tensile-strained Ge is shown in black line. The direct band gap and the indirect band gap at the same strain level is shown in red and in blue respectively. All energies are referred to the top of the valence band.

The carrier distribution and the light emission process of n-type doped 0.25% tensile-strained germanium under injection are schematically shown in Fig. 17 (a). Since the lower quantum states of the indirect  $L$  valleys are filled by electrons, the energy levels of the available states in both the direct  $\Gamma$  valley and the indirect  $L$  valleys are equal in energy. The excess electrons are injected into both valleys and the electrons in the direct  $\Gamma$  valley contribute to the direct gap light emission. The heavy n-type doping introduces free carrier absorption which negatively affects the occurrence of net gain, therefore the amount of doping should be carefully modeled and optimized.

### 3.3 Germanium gain modeling

Direct band-to-band optical transition includes three processes: optical absorption, stimulated emission, and spontaneous emission. The rate of these electron-photon scattering processes can be described by the product of scattering strength and carrier occupation probabilities. We

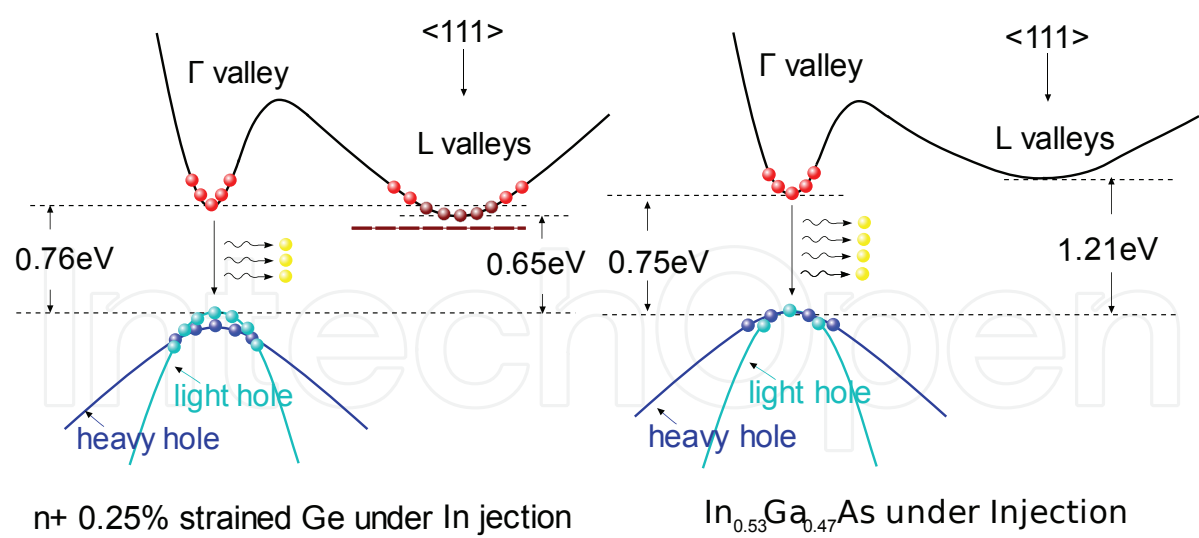


Fig. 17. Comparison of the carrier distribution and the light emission process between (a) n-type doped 0.25% tensile-strained Ge and (b)  $\text{In}_{0.53}\text{Ga}_{0.47}\text{As}$  under injection.

denote the scattering strength of absorption, stimulated emission, and spontaneous emission at photon energy  $h\nu$  are  $\alpha(h\nu)$ ,  $e_{st}(h\nu)$ , and  $e_{sp}(h\nu)$  respectively.  $\alpha(h\nu)$  is the same absorption coefficient that we calculated earlier in the photodetector section. The rate equation of carriers  $N$  related to radiative recombinations is

$$\frac{dN}{dt} = \alpha f_v(1 - f_c)N_{ph} - e_{st}f_c(1 - f_v)N_{ph} - e_{sp}f_c(1 - f_v) \tag{26}$$

where  $N_{ph}$  is the number of photons and  $f_c$  and  $f_v$  are the occupation probabilities of the electron with respect to the electron quasi Fermi level at  $E_1$  and the hole with respect to the hole quasi Fermi level at  $E_2$ , respectively. And

$$E_1 = E_c + \frac{h\nu - E_g}{1 + m_c/m_v} \text{ and } \tag{27}$$

$$E_2 = E_v - \frac{h\nu - E_g}{1 + m_v/m_c} \tag{28}$$

are the energy levels associated with the optical transition at photon energy  $h\nu$  and are related by  $E_1 - E_2 = h\nu$ . Since quasi Fermi level depends on the injection level,  $f_c$  ( $f_v$ ) is an implicit function of the density of electrons (holes) which include equilibrium electrons (holes) and injected electrons (holes).

The meaning of  $f_c(1 - f_v)$  is the joint probability of the existence of an electron at  $E_1$  in the conduction band and the absence of a hole at  $E_2$  in the valence band, which is the condition satisfied when an optical transition occurs at a given photon energy  $h\nu$ . It represents both stimulated emission and spontaneous emission. Optical absorption is the opposite process of the stimulated emission therefore  $f_v(1 - f_c)$  is used instead.

Optical gain  $g(h\nu)$  is determined by the competition of the stimulated emission and the absorption:

$$g(h\nu) = e_{st}f_c(1 - f_v) - \alpha f_v(1 - f_c). \tag{29}$$

A detailed balance analysis proves that all the three scattering strength coefficients,  $\alpha$ ,  $e_{st}$ , and  $e_{sp}$ , are equal at any photon energy  $h\nu$ . Therefore optical gain can be rewritten as

$$g(h\nu) = \alpha(f_c - f_v). \quad (30)$$

$(f_c - f_v)$  is called population inversion factor. It is negative at equilibrium or low injection indicating a net optical loss (absorption). It becomes positive at high injection, when the population of the electrons inverts indicating a net optical gain. By using the absorption data presented in the photodetector section, optical gain can be calculated with this formula.

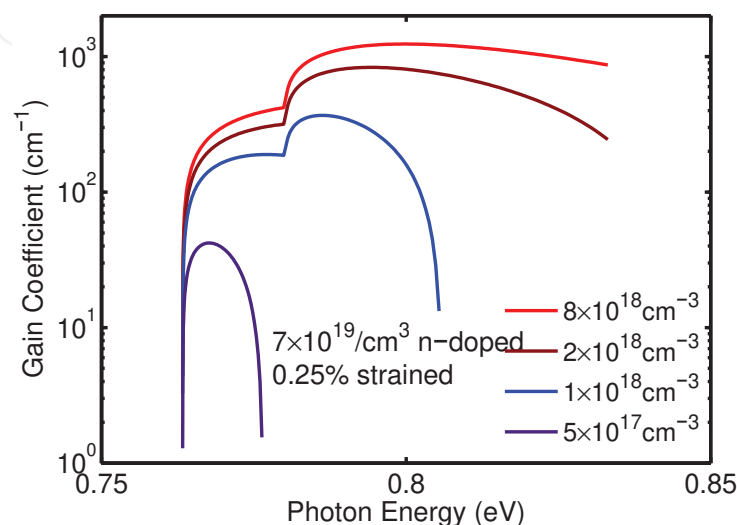


Fig. 18. Calculated optical gain spectrum of Ge with 0.25% tensile strain and  $7 \times 10^{19} \text{ cm}^{-3}$  n-type doping at various injection levels with respect to photon energies close to its direct band gap energy.

As demonstrated earlier, a combination of 0.25% tensile strain and  $7 \times 10^{19} \text{ cm}^{-3}$  n-type doping results in an effective direct band gap germanium. The optical gain spectrum of such engineered germanium is shown in Fig. 18. The optical gain occurs at 0.76 eV which is the energy gap between the direct  $\Gamma$  valley and the light-hole band under 0.25% tensile strain. Since the effective masses are very light for these bands, population inversion occurs at low injection levels of  $\sim 10^{17} \text{ cm}^{-3}$ . As the injection level increases, the separation of the electron and the hole quasi Fermi levels becomes larger than the energy gap between the direct  $\Gamma$  valley and the heavy-hole band. Thus the optical gain contributed by electron heavy-hole recombination occurs, which can be seen from the fast raise of the optical gain at 0.78 eV at injection levels above  $10^{18} \text{ cm}^{-3}$ . A peak gain over  $1000 \text{ cm}^{-1}$  around 0.8 eV (1550 nm) is achieved at injection level of  $8 \times 10^{18} \text{ cm}^{-3}$ .

The occurrence of optical gain in a material does not necessarily lead to lasing which requires that the optical gain overcomes optical losses from all sources. The material related optical loss is dominated by free carrier absorption. Free carrier absorption is a process that an electron or a hole absorbs the energy of a photon and moves to an empty higher energy state without inter-band recombination. Free carrier absorption increases with wavelength and becomes significant at high carrier densities. When a material is under carrier injection for population inversion, free carrier absorption caused by large amount of injected carriers competes against optical gain. Free carrier absorption is usually the major obstacle for lasing in a gain medium.



In n-typed doped germanium, additional free carrier absorption exists due to the existence of extrinsic electrons.

Free carrier absorption  $\alpha_{fc}$  can be expressed in the following empirical formula:

$$\alpha_{fc}(\lambda) = k_e n_c \lambda^{a_e} + k_h p_v \lambda^{a_h}, \quad (31)$$

where  $n_c$  and  $p_v$  are the densities of electrons and holes and  $k_e, k_h, a_e$  and  $a_h$  are the constants of a material.  $a_e$  and  $a_h$  are usually between 1.5 and 3.5. By fitting the free carrier absorption data in n<sup>+</sup>Ge Spitzer et al. (1961) and p<sup>+</sup>Ge Newman & Tyler (1957) in a carrier density range of  $10^{19} - 10^{20} \text{ cm}^{-3}$  at room temperature, we obtain

$$\alpha_{fc}(\lambda) = -3.4 \times 10^{-25} n_c \lambda^{2.25} - 3.2 \times 10^{-25} p_v \lambda^{2.43}, \quad (32)$$

where  $\alpha_{fc}$  is in unit of  $\text{cm}^{-1}$ ,  $n_c$  and  $p_v$  in units of  $\text{cm}^{-3}$ , and  $\lambda$  in units of nm.

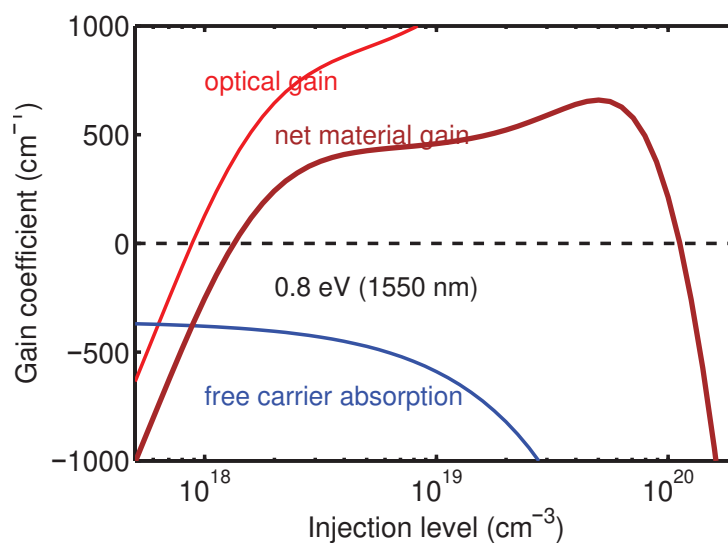


Fig. 19. The optical gain, the free carrier absorption, and the net material gain of Ge with 0.25% tensile strain and  $7 \times 10^{19} \text{ cm}^{-3}$  n-type doping at various injection levels at the photon energy of 0.8 eV (1550 nm).

The optical gain, the free carrier absorption, and the net material gain which is the difference between first two are calculated with respect to injection level at the photon energy of 0.8 eV (1550 nm) for Ge with 0.25% tensile strain and  $7 \times 10^{19} \text{ cm}^{-3}$  n-type doping. The results are shown in Fig. 19. The free carrier absorption is significant even at low injections since the material is heavily doped. The optical gain overcomes the free carrier loss above the injection level of  $1.2 \times 10^{18} \text{ cm}^{-3}$  where germanium becomes a gain medium. At very high carrier injection levels ( $> 10^{20} \text{ cm}^{-3}$ ), the free carrier absorption exceeds the optical gain leading to net loss. Between a large injection range of  $10^{18} \text{ cm}^{-3}$  and  $10^{20} \text{ cm}^{-3}$ , the tensile-strained n<sup>+</sup>Ge is a gain medium. For photon energies other than 0.8 eV, the net gain range varies but the same characteristic holds.

The comparison of the net material gain versus injection level of germanium with both tensile strain and n-type doping, with either of the two, and with neither of two are shown in Fig. 20. Since the optical gain spectrum varies with strain, the net gain for each condition is calculated at the photon energy where maximal gain is achieved. Net gain can not be achieved for intrinsic Ge no matter with or without 0.25% tensile strain because the free carrier absorption

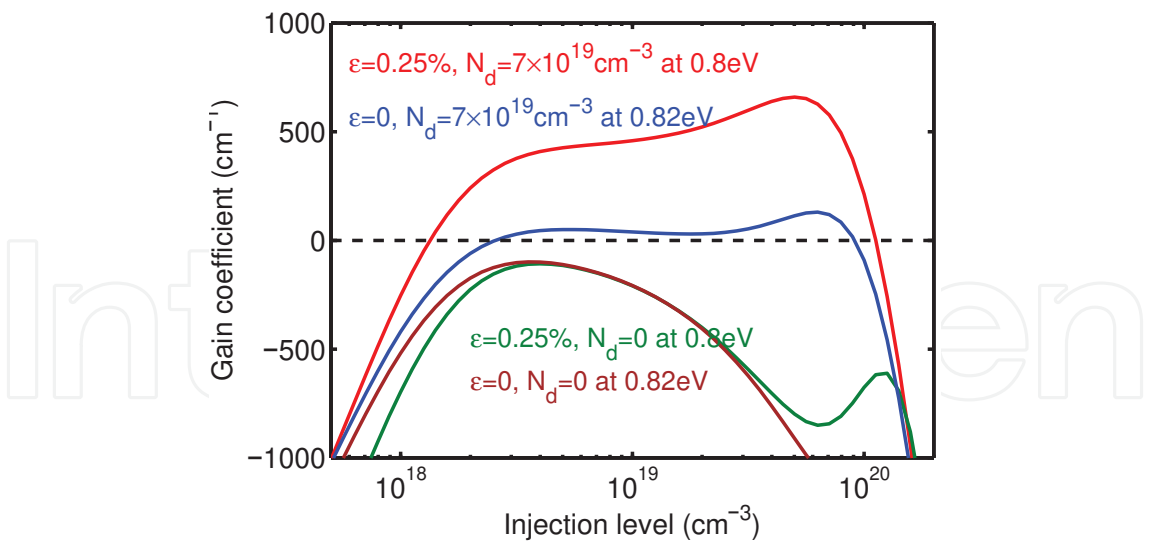


Fig. 20. Comparison of the calculated net material gain versus injection level of the Ge with both tensile strain and n-type doping, with either of two, and with neither of two at peak gain photon energy respectively.

always exceeds the optical gain. It is the reason that net gain has not been experimentally observed from germanium in the history. With n-type doping, the net gain can be achieved in both tensile-strained and unstrained cases. Tensile strain increases the population of the injected electrons in the direct  $\Gamma$  valley leading to a lower net gain threshold as well as higher net gain above threshold.

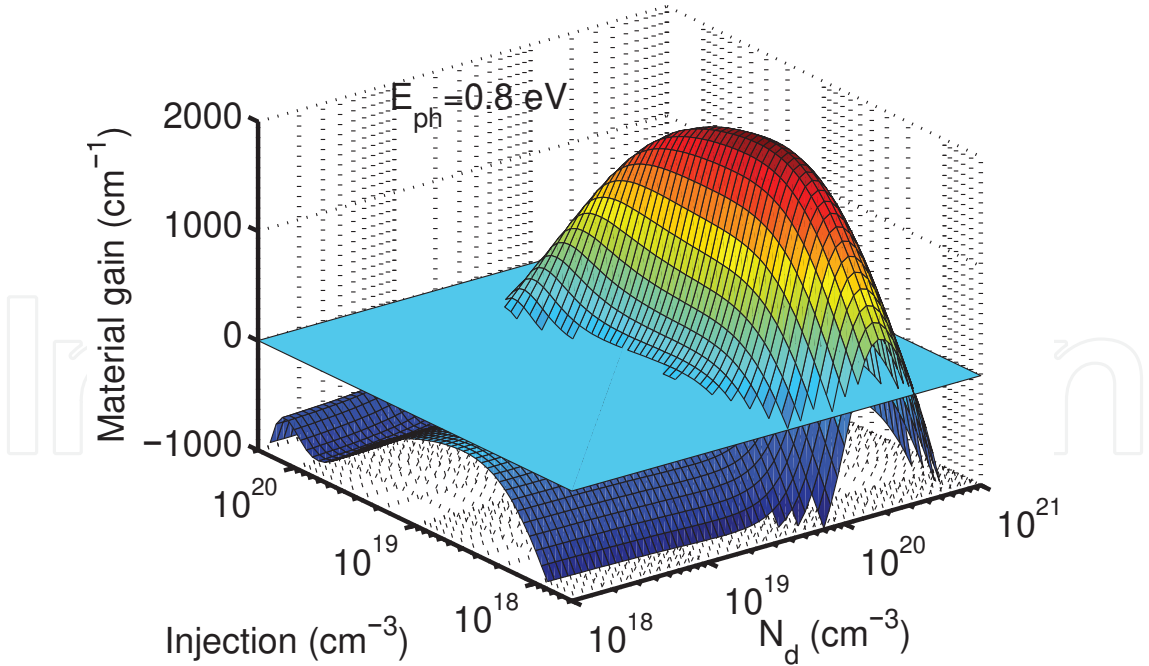


Fig. 21. Dependence of the calculated net material gain of Ge on n-type doping level ( $N_d$ ) and carrier injection level at the photon energy of 0.8 eV.

The dependence of the net gain on n-type doping level and on injection level is calculated and shown in Fig. 21. There exists a range of n-type doping concentration and carrier injection

level, in which net gain occurs. Doping concentration higher than a few  $10^{19} \text{ cm}^{-3}$  is required for net gain occurrence at photon energy of 0.8 eV. Net loss occurs at either very high doping concentrations or very high injection levels because the free carrier loss trumps the optical gain. The intercept of the 3-D plot at zero gain surface is a threshold boundary surrounding the net gain region. The threshold boundary varies at photon energies other than 0.8 eV.

### 3.4 Germanium photoluminescence and electroluminescence

Photoluminescence (PL) and electroluminescence (EL) are commonly used material characterization experiments. The intensity and spectral content of the luminescence is a direct measure of various important material properties. The carrier recombination characteristics of germanium can be studied with these experiments.

Germanium is a multi-valley indirect band gap material therefore both the direct and the indirect band-to-band radiative recombination exist. As discussed earlier indirect transition is an inefficient process as most injected electron-hole pairs recombine non-radiatively before the occurrence of radiative recombination. Therefore indirect PL can only be observed in ultra high quality germanium at cryogenic temperatures at which non-radiative recombinations are greatly suppressed. On the contrary, direct transition is a fast process with radiative recombination rate 4-5 orders of magnitude higher than that of the indirect transition (Haynes & Nilsson, 1964). However, the lack of sufficient injected electrons in the direct  $\Gamma$  valley results in weak overall light emission. The tensile strain and n-type doping techniques improve the electron concentration in the direct valley hence more efficient luminescence is expected.

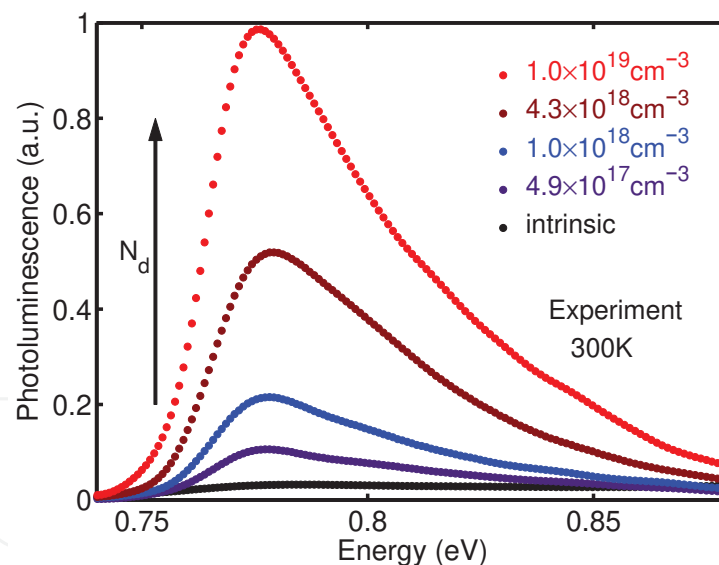


Fig. 22. PL spectra of tensile-strained Ge film with various n-type doping levels. The PL of a  $1 \times 10^{19} \text{ cm}^{-3}$  doped Ge film is over 50 times brighter than that of an undoped one. (Sun et al., 2009a)

The effect of n-type doping and tensile-strain on PL is investigated using a series of epitaxial germanium samples with doping concentrations from less than  $1 \times 10^{16} \text{ cm}^{-3}$  (approximately undoped) to  $2 \times 10^{19} \text{ cm}^{-3}$ . The doping is achieved by in situ phosphorous incorporation during germanium epitaxy. Some PL spectrum examples are shown in Fig. 22. All PL spectra are measured at room temperature. The doping dependence of PL intensities agrees with the analysis earlier that direct gap light emission is enhanced with n-type doping owing to

the indirect valley states filling with extrinsic electrons. The PL of a  $1 \times 10^{19} \text{ cm}^{-3}$  doped epitaxial germanium is over 50 times brighter than that of an undoped one. All spectra exhibit the same spectral characteristic. The same PL peak position implies that phosphorous doping has negligible effect on band structure or tensile strain in germanium.

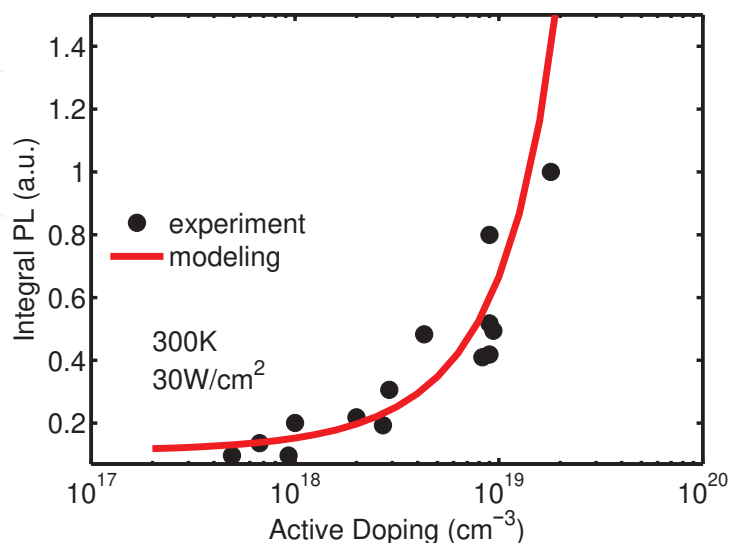


Fig. 23. A summary of integral PL intensity versus active doping concentration. The theoretical calculation is represented in red solid line and describes the trend of the experimental data.(Sun et al., 2009a)

A plot of the enhancement of integral PL intensity with active doping concentration is shown in Fig. 23. The integral PL-doping relation can be calculated by

$$I(N_d) \propto n_e^\Gamma(N_d) n_h \propto n_e^\Gamma(N_d) \quad (33)$$

It shows the direct gap integral PL intensity is proportional to the product of the electron concentration in the  $\Gamma$  valley and the hole concentration at quasi-equilibrium under excitation. The hole concentration remains the same for each sample at the same excitation level therefore the PL intensity is only determined by the electron concentration in the direct  $\Gamma$  valley. This concentration is a function of n-type doping concentration. Higher n-type doping results in more injected electrons in the direct  $\Gamma$  valley. A theoretical calculation based on this analysis is shown in Fig. 23 with red solid line, exhibiting good agreement with the experimental data. Ion-implantation is an effective way to achieve high doping concentration at the cost of crystalline damage. The lattice damages introduce defects acting as non-radiative recombination centers and reduce lifetime in materials. Fig. 24 shows the PL from epitaxial germanium implanted with phosphorus at three doses aiming for doping concentrations of  $1 \times 10^{18} \text{ cm}^{-3}$ ,  $1 \times 10^{19} \text{ cm}^{-3}$ , and  $1 \times 10^{20} \text{ cm}^{-3}$ , respectively. All samples were annealed at  $800^\circ\text{C}$  after implantation for dopant activation and subsequent Hall effect measurement confirmed over 80% dopants were activated. PL increases with the doping level in implanted germanium as expected. But all the implanted samples show weaker PL than the in situ doped one confirming the negative effect of lattice damage on radiative recombination. In general, in situ doping is a superior approach to achieve n-type doping in epitaxial germanium for light emission applications.

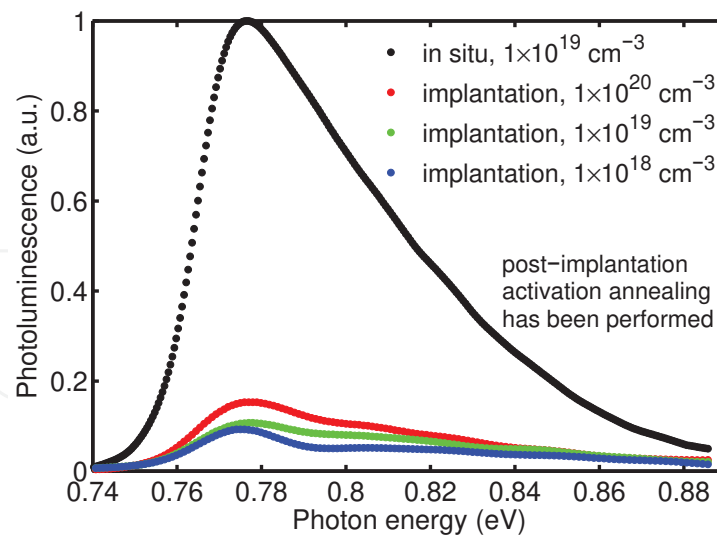


Fig. 24. PL Comparison of in situ doped Ge and implanted Ge. Post-implantation annealing has been performed for implanted Ge films for dopant activation.

Compared to PL, EL emission is excited electrically other than optically. EL is usually described as an electrical-optical phenomenon in which a material emits light in response to an electric current passed through it, or to a strong electric field. Due to different injection mechanisms, the characteristics observed in EL are not necessary the same as in PL.

Si/Ge/Si structure forms a natural heterojunction for a light-emitting diode. In the EL experiment on such Si/Ge/Si diodes, the onset of EL at forward bias has been observed at room temperature. In author's own work, EL was observed at 0.5 V forward bias or 1.3 mA injection current for a  $20 \mu\text{m}$  by  $100 \mu\text{m}$  diode.

The EL spectrum measured at room temperature at 50 mA forward current is shown in Fig. 25 (a). The EL peak is located at 0.76 eV corresponding to the direct band-to-band optical transition in 0.2% tensile-strained Ge. The full width at half maximum (FWHM) of the peak is about 60 meV ( $\sim 2 \text{ kT}$ ) consistent with the direct band-to-band transition model. The sharp peaks are from the Fabry-Perot resonance of the air gap between device surface and the flat facet of the fiber used for light collection. These resonances are reproducible in the experiments and can be filtered by fast Fourier transformation (FFT). After the FFT filtering, the smoothed curve represents the "real" EL characteristics which is shown with red solid line. The EL spectrum is consistent with the room temperature photoluminescence (PL) spectrum measured from a 0.2% tensile-strained epitaxial germanium sample shown in Fig. 25 (b). The small red shift in the EL peak position compared to PL peak position is a result of heating from current injection which slightly reduces the band gap.

The injection dependence of the direct gap EL emission was measured. The results show unique direct gap light emission characteristics of germanium which is different from that of a direct gap semiconductor.

A superlinear relation of the integral direct gap EL intensity with the injected electrical current is shown in Fig. 26. In a direct band gap semiconductor, the relation is expected to be linear at lower injection levels and to roll over at higher injection levels due to increasingly significant non-radiative recombinations. This superlinear dependence on injection is a unique feature of direct gap light emission in germanium. As discussed earlier, direct light emission intensity is



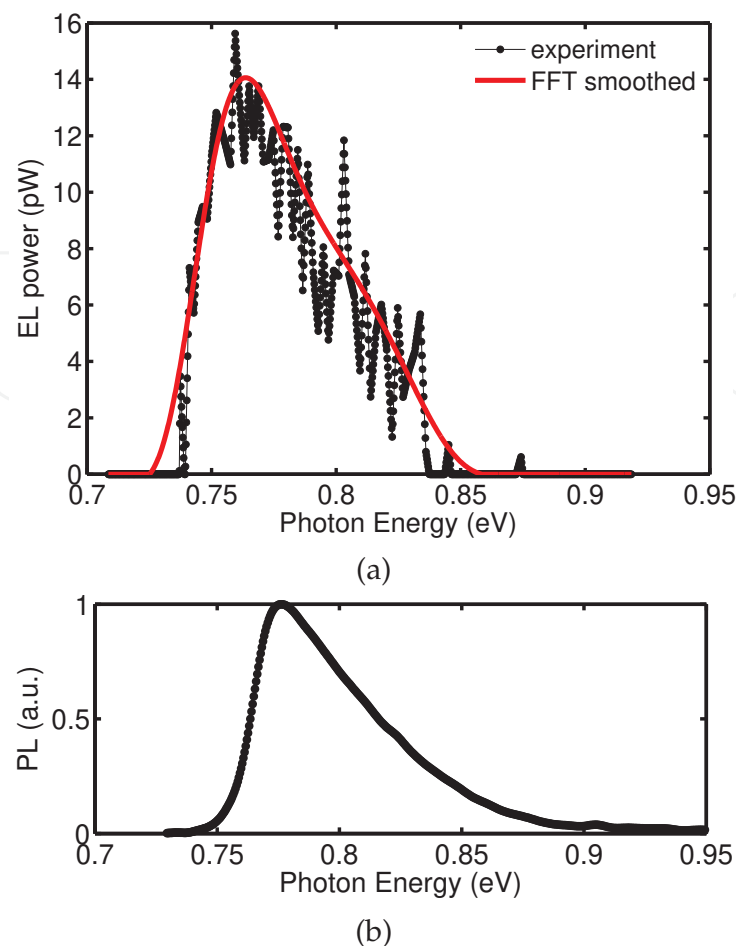


Fig. 25. (a) Direct gap EL spectrum of a 20  $\mu\text{m}$  by 100  $\mu\text{m}$  0.2% tensile-strained Si/Ge/Si light-emitting diode measured at room temperature. The periodic sharp peaks are due to Fabry-Perot resonances. (b) Room temperature direct gap photoluminescence of a 0.2% tensile-strained Ge film epitaxially grown on Si. (Sun et al., 2009b)

determined by the injected electrons in the direct  $\Gamma$  valley  $n_{e\Gamma}$  and can be further expressed as

$$P_{\Gamma} \propto n_{e\Gamma} = n_{\text{tot}} \cdot f_{\Gamma}, \quad (34)$$

where  $n_{\text{tot}}$  is the total injected electron density and  $f_{\Gamma}$  is the fraction of the electrons injected into the direct  $\Gamma$  valley. The total injected electron scales linearly with the injected electrical current. The fraction term also increases with the injection level due to the increase of the electron quasi Fermi level leading to larger portion of electrons in the direct  $\Gamma$  valley. The multiplication of the two terms results in a superlinear behavior with injection current. A theoretical calculation based on this analysis is shown in solid line in Fig. 26. It agrees well with the experimental data. The small difference between the theoretical and the experimental result is due to the small deviation from the ideal square-root density of states near the band edge.

### 3.5 Germanium net gain and lasing

It has been theoretically shown that germanium can be engineered by tensile strain and n-type doping for better direct gap light emission at room temperature. The direct gap PL and EL

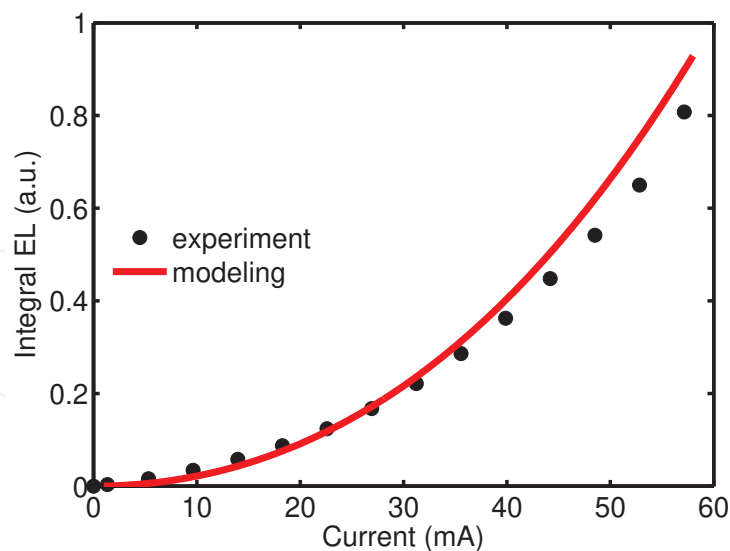


Fig. 26. Integral direct gap EL intensity of a 0.2% tensile-strained Si/Ge/Si light emitting diode. The EL intensity increases superlinearly with electrical current. The theoretical calculation (solid line) agrees well with the experimental result.

experiment greatly support this theory. Investigating the capability of net gain in germanium and to achieving lasing are next tasks.

A non-degenerate pump-probe experiment with a tunable laser as probe and a high power laser as pump is used for optical gain measurement. The fiber outputs of the pump laser and the probe laser are combined through a wavelength division multiplexing (WDM) coupler and illuminate to the top of n-type doped, tensile-strained epitaxial germanium. The transmitted optical power is measured by an integral optical sphere for transmissivity calculation with respect to incident light. The probe light is modulated at a few kHz and is filtered by a lock-in amplifier for precise transmission measurement.

The measured transmissivity is correlated with the optical gain or absorption under optical pumping:

$$g(h\nu) = \alpha(f_c - f_v). \quad (35)$$

The relation between transmissivity and optical gain/absorption can be modeled by transfer matrix method (TMM). The detailed calculated is omitted here.

The inversion factor  $(f_c - f_v)$  ranges from -1 to 1. In the absence of pumping,  $(f_c - f_v) = -1$ , i.e.  $g(h\nu) = -\alpha$  is pure absorption. As the material is increasingly pumped,  $(f_c - f_v)$  increases from -1 towards 0. The optical absorption becomes less which is called optical bleaching effect. At sufficiently high pumping levels, the material becomes transparent and a gain medium for the inversion factor equals to and more than 0, respectively.

For heavily n-type doped germanium, the measured net gain/absorption includes both optical gain/absorption and free carrier absorption:

$$g_{\text{tot}}(h\nu) = -\alpha_{\text{tot}}(h\nu) = \alpha(f_c - f_v) - \alpha_{\text{fc}}, \quad (36)$$

where  $\alpha_{\text{fc}}$  represents free carrier absorption. The existence of free carrier absorption increases the injection level required for transparency or net gain. The effective inversion factor can be expressed by

$$(f_c - f_v) - \frac{\alpha_{\text{fc}}}{\alpha} = -\frac{\alpha_{\text{tot}}}{\alpha}, \quad (37)$$

which can be obtained from the experimental results.

A tensile-strained  $n^+$  doped germanium mesa was fabricated for pump-probe measurement. The germanium is  $1.0 \times 10^{19} \text{ cm}^{-3}$   $n$ -type doped and 0.2% tensile-strained. The transmissivity spectra were measured at 0 and 60 mW optical pumping powers, respectively. The absorption is then calculated by using transfer matrix method with the consideration of Kramer-Kronig relations.

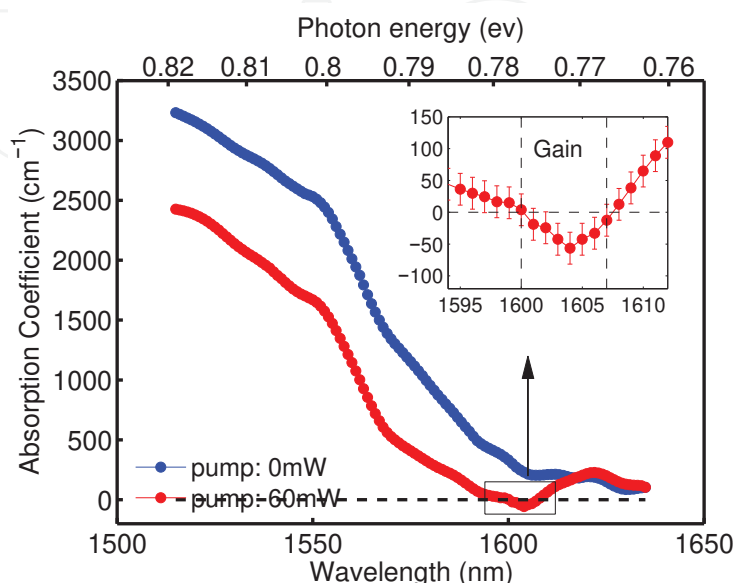


Fig. 27. The absorption spectra of the  $n^+$  Ge mesa under 0 and 60 mW optical pumping, respectively. Negative absorption corresponding to the onset of net gain was observed in wavelength between 1600 nm and 1608 nm. The error bars in the inset represent the transmissivity measurement errors. Liu et al. (2009).

Fig. 27 shows the absorption spectra of the  $n^+$  Ge mesa under pumping powers of 0 and 60W, respectively. The absorption at photon energies above 0.77 eV (at wavelengths below 1610 nm) decreases significantly upon optical pumping. Negative absorption corresponding to the onset of optical gain is observed in the wavelength range of 1600-1608 nm, as shown in the inset of Fig. 27. The maximum gain coefficient is  $g_{\text{tot}} = -\alpha_{\text{tot}} = 50 \pm 25 \text{ cm}^{-1}$  at 1605 nm. The error bars represent the transmissivity measurement errors.

Like PL in doped germanium, the optical bleaching effect also increases with the  $n$ -type doping concentration. The effective inversion factor is calculated from the experimental results for germanium with different doping concentrations.

The comparison of the effective inversion factor spectra of tensile-strained Ge for both blanket film and mesa samples with various  $n$ -type doping concentrations is shown in Fig. 28. The optical bleaching effect (inversion factor more than -1) can be seen from all samples. The bleaching increases with  $n$ -type doping concentration confirming the theory of the effect of  $n$ -type doping on optical gain. The Ge mesa sample exhibits a positive inversion factor at the direct band edge (1600-1608 nm) underlying the occurrence of net gain. The effective inversion factors at longer wavelengths are less than -1 for all samples because free carrier absorption overcomes optical bleaching. The optical bleaching in the Ge mesa sample is more than any Ge film samples as a result of the lateral confinement of injected carriers by the mesa structure. With the observation of net gain in tensile-strained  $n$ -doped germanium, an optically pumped Fabry-Perot germanium laser was realized (Liu et al., 2010). The waveguide laser was excited

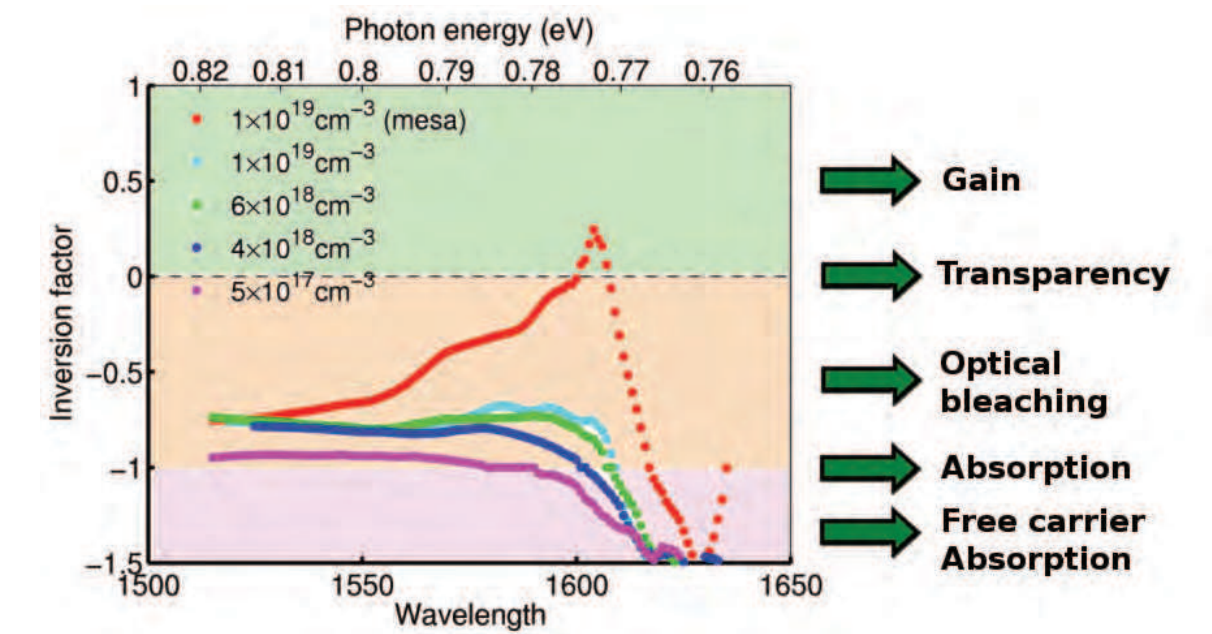


Fig. 28. Comparison of the effective inversion factors of tensile-strained Ge film and mesa with various n-type doping concentrations. The observed optical bleaching effect increases with n-type doping concentration.

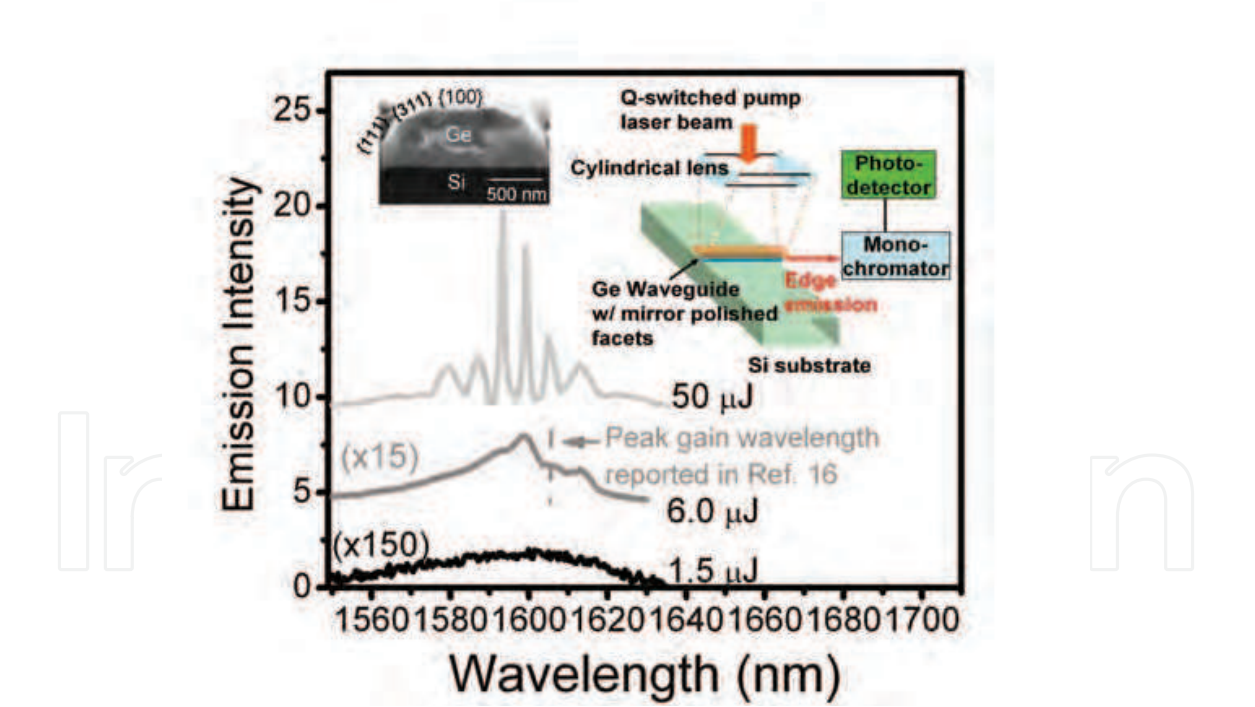


Fig. 29. Edge emission spectra of a Ge waveguide with mirror polished facets under excitation. The three spectra at 1.5, 6.0 and 50  $\mu\text{J}$ /pulse pumping power correspond to spontaneous emission, threshold for lasing, and laser emission, respectively. The inset shows a cross-sectional SEM picture of the Ge waveguide and a schematic drawing of the experimental setup for optical pumping.

by a 1064 nm Q-switched laser through a cylindrical focusing lens. The lasing measurement is schematically shown in the inset of Fig. 29. The light emission spectra of the laser under different injection levels are shown in Fig. 29. At 1.5  $\mu\text{J}/\text{pulse}$  of pump laser power, the spectrum is a typical spontaneous emission consistent with PL results discussed earlier. As the pump power increases to 6.0  $\mu\text{J}/\text{pulse}$ , a few peaks emerge which occurs at the pump power corresponding to the threshold condition in Fig. 30. It marks the onset of transparency. The occurrence of emission peaks between 1600 and 1610 nm is consistent with the optical gain spectrum peaked at 1605 nm shown earlier. As pump power increases to 50  $\mu\text{J}/\text{pulse}$ , the widths of the emission peaks at 1594, 1599 and 1605 nm significantly decrease and the polarization became to predominant TE other than a mixture of TE and TM at lower injections. These results represent a typical lasing behavior. The multiple emission peaks are most likely due to multiple guided modes in the germanium waveguide as a result of high refractive index contrast. A similar multimode behavior has been observed in an early work on III-V semiconductor lasers (Miller et al., 1977).

Fig. 30 shows the integral edge emission intensity as a function of pump power. An obvious threshold behavior is observed. The threshold pumping power is about 5  $\mu\text{J}/\text{pulse}$ . The absorbed pump power density at the threshold is about 30  $\text{kW}/\text{cm}^2$  by considering various optical losses of the incident pump light. The threshold is expected to further decrease with increased n-type doping concentration based on the calculation earlier. With lower injection threshold requirement, an electrically pumped germanium laser diode can be realized. As shown in the EL experiment discussion, Ge/Si/Ge heterojunction may be suitable diode structure for such lasers which will eventually complete the integrated silicon photonic circuits for the next generation of data communication and interconnects.

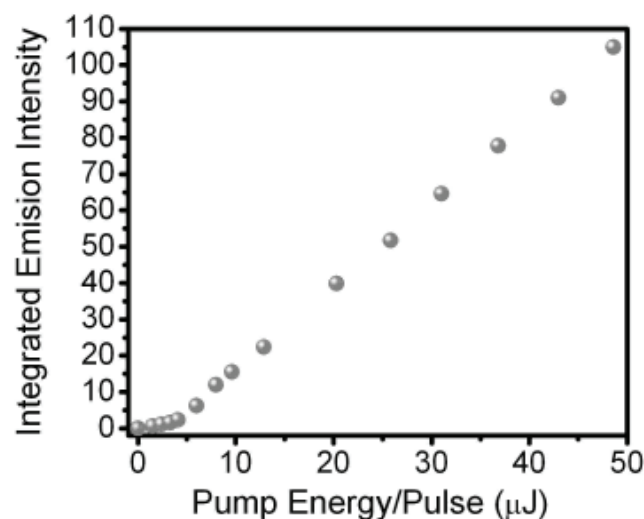


Fig. 30. Integral edge emission power versus optical pump power showing a lasing threshold behavior.

#### 4. References

- Adeola, G. W., Jambois, O., Miska, P., Rinnert, H. & Vergnat, M. (2006). Luminescence efficiency at 1.5  $\mu\text{m}$  of er-doped thick sio layers and er-doped sio / sio2 multilayers, *Appl. Phys. Lett.* 89: 101920.



- Ahn, D., Yin Hong, C., Liu, J., Giziewicz, W., Beals, M., Kimerling, L. C. & Michel, J. (2007). High performance, waveguide integrated Ge photodetectors, *Opt. Express* 15(7): 3916–3921.
- Aicher, W. & Habberger, K. (1999). Influence of optical interconnects at the chip and board levels, *Opt. Eng.* 38: 313–322.
- Bean, J. C., Sheng, T. T., I. C. Feldman, Fiory, A. T. & Lynch, R. T. (1984). Pseudomorphic growth of  $\text{Ge}_{x\text{Si}_{1-x}}$  on silicon by molecular beam epitaxy, *Appl. Phys. Lett.* 44: 102.
- Boyratz, O. & Jalali, B. (2004). Demonstration of a silicon Raman laser, *Opt. Express* 12(21): 5269–5273.
- Braunstein, R., Moore, A. R. & Herman, F. (1958). Intrinsic optical absorption in germanium-silicon alloys, *Phys. Rev.* 109(3): 695–710.
- Cannon, D. D., Liu, J., Ishikawa, Y., Wada, K., Danielson, D. T., Jongthammanurak, S., Michel, J. & Kimerling, L. C. (2004). Tensile strained epitaxial Ge films on Si(100) substrates with potential application in L-band telecommunications, *Appl. Phys. Lett.* 84(6): 906–908.
- Chuang, S. L. (1995). *Physics of Optoelectronic Devices*, John Wiley & Sons. Inc, chapter 4, p. 144.
- Colace, L., Balbi, M., Masini, G., Assanto, G., Luan, H.-C. & Kimerling, L. C. (n.d.). Ge on si p-i-n photodiodes operating at 10 gbit/s, *Appl. Phys. Lett.* 88: 101111.
- Colace, L., Masini, G., Altieri, A. & Assanto, G. (2006). Waveguide photodetectors for the near-infrared in polycrystalline germanium on silicon, *IEEE Photon. Technol. Lett.* 18: 1094.
- Colace, L., Masini, G., Assanto, G., Luan, H.-C., Wada, K. & Kimerling, L. C. (2000). Efficient high-speed near-infrared Ge photodetectors integrated on Si substrates, *Appl. Phys. Lett.* 76(10): 1231.
- Colace, L., Masini, G., Galluzzi, F., Assanto, G., Capellini, G., Gaspare, L. D., & Evangelisti, F. (1997). Ge/Si (001) photodetector for near infrared light, *Solid State Phenom.* 54: 55.
- Colace, L., Masini, G., Galluzzi, F., Assanto, G., Capellini, G., Gaspare, L. D., Palange, E. & Evangelisti, F. (1998). Metal-semiconductor-metal near-infrared light detector based on epitaxial Ge/Si, *Appl. Phys. Lett.* 72(24): 3175–3177.
- Currie, M. T., Samavedam, S. B., Langdo, T. A., Leitz, C. W. & Fitzgerald, E. A. (1998). Controlling threading dislocation densities in Ge on Si using graded SiGe layers and chemical-mechanical polishing, *Appl. Phys. Lett.* 72: 1718–1720.
- Dash, W. C. & Newman, R. (1955). Intrinsic optical absorption in single-crystal germanium and silicon at 77 Å and 300 Å, *Phys. Rev.* 99(4): 1151–1155.
- de Walle, C. G. V. (1989). Band lineups and deformation potentials in the model-solid theory, *Phys. Rev. B* 39(3): 1871–1883.
- Dehlinger, G., Koester, S. J., Schaub, J. D., Chu, J. O., Ouyang, Q. C. & Grill, A. (2004). High-Speed Germanium-on-SOI Lateral PIN Photodiodes, *IEEE Photon. Technol. Lett.* 16(11): 2547–2549.
- Eaglesham, D. J., Unterwald, F. C. & Jacobson, D. C. (1993). Growth morphology and the equilibrium shape: the role of surfactants in Ge/Si island formation, *Phys. Rev. Lett.* 70(7): 966–969.
- Fama, S., Colace, L., Masini, G., Assanto, G. & Luan, H.-C. (n.d.). High performance germanium-on-silicon detectors for optical communications, *Appl. Phys. Lett.* 81(4): 586.
- Fang, A. W., Park, H., Cohen, O., Jones, R., Paniccia, M. J. & Bowers, J. E. (2006). Electrically pumped hybrid AlGaInAs-silicon evanescent laser, *Opt. Express* 14(20): 9203–9210.

- Fang, Y.-Y., Tolle, J., Roucka, R., Chizmeshya, A. V. G., Kouvetakis, J., D'Costa, V. R. & Menendez, J. (2007). Perfectly tetragonal, tensile-strained ge on  $\text{ge}_{1-y}\text{sn}_y$  buffered si(100), *Appl. Phys. Lett.* 90: 061915.
- Feng, D., Liao, S., Dong, P., Feng, N.-N., Liang, H., Zheng, D., Kung, C.-C., Fong, J., Shafiiha, R., Cunningham, J., Krishnamoorthy, A. V., & Asghari, M. (2009). High-speed ge photodetector monolithically integrated with large cross-section silicon-on-insulator waveguide, *Appl. Phys. Lett.* 95: 261105.
- Feng, N.-N., Dong, P., Zheng, D., Liao, S., Liang, H., Shafiiha, R., Feng, D., Li, G., Cunningham, J. E., V.Krishnamoorthy, A. & Asghari, M. (2010). Vertical p-i-n germanium photodetector with high external responsivity integrated with large core si waveguides, *Optics Express* 18(1): 96.
- Fidaner, O., Okayay, A. K., Roth, J. E., Schaevitz, R. K., Kuo, Y.-H., Saraswat, K. C., James S. Harris, J. & Miller, D. A. B. (2007). Ge $\delta$  quantum-well waveguide photodetectors on silicon for the near-infrared, *IEEE Photon. Technol. Lett.* 19(20): 1631.
- Fitzgerald, E. A., Xie, Y.-H., Green, M. L., Brasen, D., Kortan, A. R., Michel, J., Mii, Y.-J. & Weir, B. E. (1991). Totally relaxed  $\text{ge}_x\text{si}_{1-x}$  layers with low threading dislocation densities grown on si substrates, *Appl. Phys. Lett.* 59(7): 811–813.
- Frova, A. & Handler, P. (1965). Franz-keldysh effect in the space-charge region of a germanium p-n junction, *Phy. Rev.* 137(6A): A1857–A1861.
- Fujii, M., Yoshida, M., Kanzawa, Y., Hayashi, S. & Yamamoto, K. (1997). 1.54  $\mu\text{m}$  photoluminescence of  $\text{er}^{3+}$  doped into  $\text{siO}_2$  films containing si nanocrystals: Evidence for energy transfer from si nanocrystals to  $\text{er}^{3+}$ , *Appl. Phys. Lett.* 71(9): 1198–1200.
- Garozzo, M., Conte, G., Evangelisti, F. & Vitali, G. (1982). Heteroepitaxial growth of ge on  $\langle 111 \rangle$  si by vacuum evaporation, *Appl. Phys. Lett.* 41: 1070.
- Gelloz, B. & Koshida, N. (2000). Electroluminescence with high and stable quantum efficiency and low threshold voltage from anodically oxidized thin porous silicon diode, *J. Appl. Phys.* 88(7): 4319–4324.
- Groenert, M. E., Leitz, C. W., Pitera, A. J., Yang, V., Lee, H., Ram, R. & Fitzgerald, E. A. (2003). Monolithic integration of room-temperature cw GaAs/AlGaAs lasers on Si substrates via relaxed graded GeSi buffer layers, *J. Appl. Phys.* 93(1): 362–367.
- Haensch, W., Nowak, E. J., Dennard, R. H., Solomon, P. M., Bryant, A., Dokumaci, O. H., Kumar, A., Wang, X., Johnson, J. B. & Fischetti, M. V. (2006). Silicon cmos devices beyond scaling, *IBM J. Res. & Dev.* 50: 339–361.
- Han, H.-S., Seo, S.-Y. & Shin, J. H. (2001). Optical gain at 1.54  $\mu\text{m}$  erbium-doped silicon nanocluster sensitized waveguide, *Appl. Phys. Lett.* 79(27): 4568–4570.
- Hartmann, J. M., Abbadie, A., Papon, A. M., Holliger, P., Rolland, G., Billon, T., Fedeli, J. M., Rouviere, M., Vivien, L. & Laval, S. (2004). Reduced pressure-chemical vapor deposition of ge thick layers on si(001) for 1.3–1.55  $\mu\text{m}$  photodetection, *J. Appl. Phys.* 95: 5905.
- Haurylau, M., Chen, G., Chen, H., Zhang, J., Nelson, N. A., Albonesi, D. H., Friedman, E. G. & Fauchet, P. M. (2006). On-chip optical interconnect roadmap: Challenges and critical directions, *IEEE J. Sel. Topic Quantum Electron.* 12(6): 1699–1705.
- Haynes, J. R. & Nilsson, N. G. (1964). The direct radiative transitions in germanium and their use in the analysis of lifetime, *Proceedings of VIIth International Conference on Physics of Semiconductors*, Paris, p. 21.

- Hobden, M. V. (1962). Direct optical transitions from the split-off valence band to the conduction band in germanium, *J. Phys. Chem. Solids* 23(6): 821–822.
- Iacona, F., Pacifici, D., Irrera, A., Miritello, M., Franzo, G. & Priolo, F. (2002). Electroluminescence at 1.54  $\mu\text{m}$  in er-doped si nanocluster-based devices, *Appl. Phys. Lett.* 81(17): 3242–3244.
- Irrera, A., Pacifici, D., Miritello, M., Franzo, G., Priolo, F., Iacona, F., Sanfilippo, D., Stefano, G. D. & Fallica, P. G. (2003). Electroluminescence properties of light emitting devices based on silicon nanocrystals, *Physica E* 16(3-4): 395–399.
- Jacoboni, C., Nava, F., Canali, C. & Ottaviani, G. (1981). Electron drift velocity and diffusivity in germanium, *Phys. Rev. B* 24(2): 1014–1026.
- Kamins, T. I. & Meyer, D. J. (1991). *Appl. Phys. Lett.* 59: 178.
- Kasper, E. & Herzog, H.-J. (1977). Elastic strain and misfit dislocation density in  $\text{Si}_{0.92}\text{Ge}_{0.08}$  films on silicon substrates, *Thin Solid Films* 44: 357.
- Kik, P. G., Brongersma, M. L. & Polman, A. (2000). Strong exciton-erbium coupling in si nanocrystal-doped  $\text{SiO}_2$ , *Appl. Phys. Lett.* 76(17): 2325–2327.
- Kirchain, R. & Kimerling, L. C. (2007). A roadmap for nanophotonics, *Nature Photonics* 1: 303–305.
- Kobayashi, S., Cheng, M.-L., Kohlhase, A., Sato, T., Murota, J. & Mikoshiba, N. (1990). Selective germanium epitaxial growth on silicon using cvd technology with ultra-pure gases, *J. Crystal Growth* 99: 259.
- Koshida, N. & Koyama, H. (1992). Visible electroluminescence from porous Si, *Appl. Phys. Lett.* 60(3): 347–349.
- Langdo, T. A., Leitz, C. W., Currie, M. T., Fitzgerald, E. A., Lochtefeld, A. & Antoniadis, D. A. (2000). High quality ge on si by epitaxial necking, *Appl. Phys. Lett.* 75(25): 3700–3702.
- Leong, D., Harry, M., Reeson, K. J. & Homewood, K. P. (1997). A silicon/iron-disilicide light-emitting diode operating at a wavelength of 1.5  $\mu\text{m}$ , *Nature* 387(6634): 686–688.
- Lipson, M. (2004). Overcoming the limitations of microelectronics using Si nanophotonics: solving the coupling, modulation and switching challenges, *Nanotechnology* 15(10): S622–S627.
- Liu, J., Cannon, D. D., Wada, K., Ishikawa, Y., Jongthammanurak, S., Danielson, D. T., Michel, J. & Kimerling, L. C. (2005). Tensile strained ge p-i-n photodetectors on si platform for c and l band telecommunications, *Appl. Phys. Lett.* 87(1): 011110.
- Liu, J., Cannon, D., Ishikawa, Y., Wada, K., Danielson, D. T., Jongthammanurak, S., Michel, J. & Kimerling, L. C. (2004). Deformation potential constants of biaxially tensile stressed ge epitaxial films on si(100), *Phys. Rev. B* 70(15): 155309.
- Liu, J., Michel, J., Giziewicz, W., Pan, D., Wada, K., Cannon, D. D., Jongthammanurak, S., Danielson, D. T., Kimerling, L. C., Chen, J., Ilday, F. O., Kartner, F. X. & Yasaitis, J. (2005). High-performance, tensile-strained Ge p-i-n photodetectors on a Si platform, *Appl. Phys. Lett.* 87(10): 103501.
- Liu, J., Sun, X., Camacho-Aguilera, R., Kimerling, L. C. & Michel, J. (2010). Ge-on-si laser operating at room temperature, *Optics Lett.* 35(5): 679.
- Liu, J., Sun, X., Kimerling, L. C. & Michel, J. (2009). Direct band gap photoluminescence and onset of optical gain of band-engineered ge-on-si at room temperature, *Optics Lett.* . accepted.
- Liu, Y., Deal, M. D. & Plummer, J. D. (2004). High-quality single-crystal ge on insulator by liquid-phase epitaxy on si substrates, *Appl. Phys. Lett.* 84: 2563.

- Luan, H.-C., Lim, D. R., Lee, K. K., Chen, K. M., Sandland, J. G., Wada, K. & Kimerling, L. C. (1999). High-quality Ge epilayers on Si with low threading-dislocation densities, *Appl. Phys. Lett.* 75(19): 2909–2911.
- Luan, H.-C., Wada, K., Kimerling, L. C., Masini, G., Colace, L. & Assanto, G. (2001). High efficiency photodetectors based on high quality epitaxial germanium grown on silicon substrates, *Optical Mater.* 17: 71.
- Luryi, S., Kastalsky, A. & Bean, J. C. (1984). New infrared detector on a silicon chip, *IEEE Trans. Electron. Dev.* 31: 1135.
- Madelung, O. & et al (eds) (1982). *Properties of Group IV Elements and III-V, II-VI, and I-VII Compounds*, Vol. 17a, Springer, Berlin.
- Makarova, M., Sih, V., Warga, J., Li, R., Negro, L. D. & Vuckovic, J. (2008). Enhanced light emission in photonic crystal nanocavities with Erbium-doped silicon nanocrystals, *Appl. Phys. Lett.* 92(16): 161107.
- Masini, G., Capellini, G., Witzens, J. & Gunn, C. (2007). A 1550nm, 10Gbps monolithic optical receiver in 130nm CMOS with integrated Ge waveguide photodetector, *4th IEEE International Conference on Group IV Photonics*, Tokyo, Japan, pp. 19–21.
- Meyerson, B. S. (1986). Low-temperature silicon epitaxy by ultrahigh vacuum chemical vapor deposition, *Appl. Phys. Lett.* 48: 797–799.
- Meyerson, B. S. (1990). Low-temperature si and sige epitaxy by ultrahigh-vacuum chemical deposition: process fundamentals, *IBM J. Res. Develop* 34(6): 806–815.
- Meyerson, B. S. (1992). Uhvcvd growth of si and sige alloys: chemical, physics, and device applications, *Proc. IEEE* 80(10): 1592–1608.
- Miller, K. J. & Grieco, M. J. (1962). Epitaxial silicon-germanium alloy films on silicon substrates, *J. Electrochem. Society* 109: 70.
- Miller, R. C., Nordland, W. A., Logan, R. A. & Johnson, L. F. (1977). Optically pumped taper-coupled gaas-algaas laser with a second-order bragg reflector, *J. Appl. Phys* 49: 539.
- M. Levinstein, Rumyantsev, S. & Shur, M. (eds) (1996). *Handbook Series on Semiconductor Parameters*, World Scientific.
- Moore, G. (1965). Cramming more components onto integrated circuits, *Electronics* 38: 144–147.
- Morse, M., Dosunmu, O., Sarid, G. & Chetrit, Y. (2006). Performance of ge-on-si p-i-n photodetectors for standard receiver modules, *IEEE Photon. Technol. Lett.* 18: 2442.
- Muller, D. A. (2005). A sound barrier for silicon?, *Nature Mater.* 4: 645–647.
- Nazarov, A., Sun, J. M., Skorupa, W., Yankov, R. A., Osiyuk, I. N., Tjagulskii, I. P., Lysenko, V. S. & Gebel, T. (2005). Light emission and charge trapping in er-doped silicon dioxide films containing silicon nanocrystals, *Appl. Phys. Lett.* 86: 151914.
- Negro, L. D., Li, R., Warga, J. & Basu, S. N. (2008). Sensitized erbium emission from silicon-rich nitride/silicon superlattice structures, *Appl. Phys. Lett.* 92(18): 181105.
- Newman, R. & Tyler, W. W. (1957). Effect of impurities on free-hole infrared absorption in p-type germanium, *Phys. Rev.* 105: 885–886.
- O'Connor, I., Tissafi-Drissi, F., Gaffiot, F., Dambre, J., Wilde, M. D., Campenhout, J. V., Thourhout, D. V., Campenhout, J. V. & Stroobandt, D. (2007). Systematic simulation-based predictive synthesis of integrated optical interconnect, *IEEE Trans. VLSI Sys.* 15: 927–940.
- O'Connor, I., Tissafi-Drissi, F., Navarro, D., Mieyeville, F., Gaffiot, F., Dambre, J., Wilde, M. D., Stroobandt, D. & Briere, M. (2006). Integrated optical interconnect for on-chip data

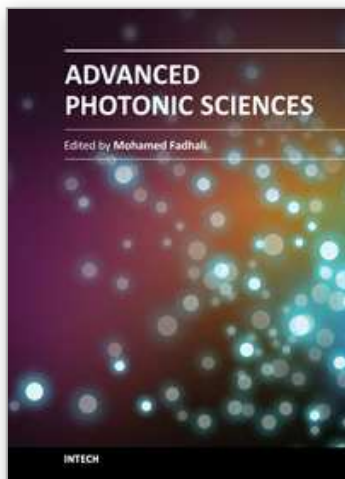


- transport, *Circuits and Systems, 2006 IEEE North-East Workshop on*, Gatineau, Que., p. 209.
- Okada, Y. & Tokumaru, Y. (1984). Precise determination of lattice parameter and thermal expansion coefficient of silicon between 300 and 1500 K, *J. Appl. Phys.* 56: 314.
- Osmond, J., Isella, G., Chrestina, D., Kaufmann, R., Acciarri, M. & von Kanel, H. (2009). Ultralow dark current Ge/Si(100) photodiodes with low thermal budget, *Appl. Phys. Lett.* 94: 201106.
- Park, H., Fang, A. W., Kodama, S. & Bowers, J. E. (2005). Hybrid silicon evanescent laser fabricated with a silicon waveguide and III-V offset quantum wells, *Opt. Express* 13(23): 9460–9464.
- Peng, C. S., Huang, Q., Cheng, W. Q., Zhou, J. M., Zhang, Y. H., Sheng, T. T. & Tung, C. H. (1998). Optical properties of Ge self-organized quantum dots in Si, *Phys. Rev. B* 57: 8805–8808.
- Polman, A., Min, B., Kalkman, J., Kippenberg, T. J. & Vahala, K. J. (2004). Ultralow-threshold erbium-implanted toroidal microlaser on silicon, *Appl. Phys. Lett.* 84(7): 1037–1039.
- Raider, S. I., Flitsch, R. & Palmer, M. J. (1975). Oxide growth on etched silicon in air at room temperature, *J. Electrochem. Soc.* 12: 413.
- Rong, H., Jones, R., Liu, A., Cohen, O., Hak, D., Fang, A. & Paniccia, M. (2005). A continuous-wave Raman silicon laser, *Nature* 433: 725–728.
- Rong, H., Liu, A., Jones, R., Cohen, O., Hak, D., Nicolaescu, R., Fang, A. & Paniccia, M. (2004). An all-silicon Raman laser, *Nature* 433(1): 292–294.
- Samavedam, S. B., Currie, M. T., Langdo, T. A. & Fitzgerald, E. A. (1998). High-quality germanium photodiodes integrated on silicon substrates using optimized relaxed graded buffers, *Appl. Phys. Lett.* 73(15): 2125.
- Samavedam, S. B. & Fitzgerald, E. A. (1997). Novel dislocation structure and surface morphology effects in relaxed Ge/Si-Ge(graded)/Si structures, *J. Appl. Phys.* 81(7): 3108–3116.
- Singh, H. P. (1968). Determination of thermal expansion of germanium, rhodium, and iridium by x-rays, *Acta Crystallogr., Sect. A: Cryst. Phys., Diffraction, Theor. Gen. Crystallogr.* 24: 469–471.
- Spitzer, W. G., Trumbore, F. A. & Logan, R. A. (1961). Properties of heavily doped n-type germanium, *J. Appl. Phys.* 32: 1822–1830.
- Sun, X., Liu, J., Kimerling, L. C. & Michel, J. (2009a). Direct gap photoluminescence of n-type tensile-strained Ge-on-Si, *Appl. Phys. Lett.* . in review.
- Sun, X., Liu, J., Kimerling, L. C. & Michel, J. (2009b). Room temperature direct band gap electroluminescence from Ge-on-Si light emitting diodes, *Optics Lett.* 34(8): 1198–1200.
- Sutter, P., Kafader, U. & von Kanel, H. (1994). Thin film photodetectors grown epitaxially on silicon, *Solar Energy Mater. Solar Cell* 31: 541.
- Tsaur, B.-Y., Geis, M. W., Fan, J. C. C. & Gale, R. P. (1981). Heteroepitaxy of vacuum-evaporated Ge films on single-crystal Si, *Appl. Phys. Lett.* 38: 779.
- Vivien, L., Osmond, J., Fedeli, J.-M., Marris-Morini, D., and Jean-Francois Damlencourt, P. C., Cassan, E., Y.Lecunff & Laval, S. (2009). 42 GHz p.i.n germanium photodetector integrated in a silicon-on-insulator waveguide, *Optics Express* 17(8): 6252.
- Vivien, L., Rouviere, M., Fedeli, J.-M., Marris-Morini, D., Damlencourt, J.-F., Mangeney, J., Crozat, P., Melhaoui, L. E., Cassan, E., Roux, X. L., Pascal, D. & Laval, S. (2007). High speed and high responsivity germanium photodetector integrated in a Silicon-On-Insulator microwaveguide, *Opt. Express* 15(15): 9843.



- Vossen, J. L., Thomas, J. H., Maa, J. S. & O'Neill, J. J. (1984). Preparation of surfaces for high quality interface formation, *J. Vac. Sci. Technol. A* 2: 212–215.
- Wang, J., Loh, W. Y., Chua, K. T., Zang, H., Xiong, Y. Z., Loh, T. H., Yu, M. B., Lee, S. J., Lo, G.-Q. & Kwong, D.-L. (2008). Evanescent-coupled ge p-i-n photodetectors on si-waveguide with seg-ge and comparative study of lateral and vertical p-i-n configurations, *IEEE Electron Dev. Lett.* 29(5): 445.
- Wang, J., Loh, W. Y., Chua, K. T., Zang, H., Xiong, Y. Z., Tan, S. M. F., Yu, M. B., Lee, S. J., Lo, G. Q. & Kwong, D.-L. (2008). Low-voltage high-speed (18 ghz/1 v) evanescent-coupled thin-film-ge lateral pin photodetectors integrated on si waveguide, *IEEE Photon. Technol. Lett.* 20(17): 1485.
- Yin, T., Cohen, R., Morse, M. M., Sarid, G., Chetrit, Y., Rubin, D. & Paniccia, M. J. (2007). 31GHz Ge n-i-p waveguide photodetectors on Silicon-on-Insulator substrate, *Opt. Express* 15(21): 13965–13971.
- Zhang, B., Michel, J., Ren, F. Y. G., Kimerling, L. C., Jacobson, D. C. & Poate, J. M. (1994). Room-temperature sharp line electroluminescence at  $\lambda=1.54 \mu\text{m}$  from an erbiqm-doped, silicon light-emitting diode, *Appl. Phys. Lett.* 64(21): 2842–2844.

IntechOpen



### **Advanced Photonic Sciences**

Edited by Dr. Mohamed Fadhal

ISBN 978-953-51-0153-6

Hard cover, 374 pages

**Publisher** InTech

**Published online** 21, March, 2012

**Published in print edition** March, 2012

The new emerging field of photonics has significantly attracted the interest of many societies, professionals and researchers around the world. The great importance of this field is due to its applicability and possible utilization in almost all scientific and industrial areas. This book presents some advanced research topics in photonics. It consists of 16 chapters organized into three sections: Integrated Photonics, Photonic Materials and Photonic Applications. It can be said that this book is a good contribution for paving the way for further innovations in photonic technology. The chapters have been written and reviewed by well-experienced researchers in their fields. In their contributions they demonstrated the most profound knowledge and expertise for interested individuals in this expanding field. The book will be a good reference for experienced professionals, academics and researchers as well as young researchers only starting their carrier in this field.

### **How to reference**

In order to correctly reference this scholarly work, feel free to copy and paste the following:

Xiaochen Sun (2012). Germanium-on-Silicon for Integrated Silicon Photonics, Advanced Photonic Sciences, Dr. Mohamed Fadhal (Ed.), ISBN: 978-953-51-0153-6, InTech, Available from:  
<http://www.intechopen.com/books/advanced-photonic-sciences/integrated-photonics-in-silicon-and-germanium>

**INTeCH**  
open science | open minds

### **InTech Europe**

University Campus STeP Ri  
Slavka Krautzeka 83/A  
51000 Rijeka, Croatia  
Phone: +385 (51) 770 447  
Fax: +385 (51) 686 166  
[www.intechopen.com](http://www.intechopen.com)

### **InTech China**

Unit 405, Office Block, Hotel Equatorial Shanghai  
No.65, Yan An Road (West), Shanghai, 200040, China  
中国上海市延安西路65号上海国际贵都大饭店办公楼405单元  
Phone: +86-21-62489820  
Fax: +86-21-62489821

© 2012 The Author(s). Licensee IntechOpen. This is an open access article distributed under the terms of the [Creative Commons Attribution 3.0 License](https://creativecommons.org/licenses/by/3.0/), which permits unrestricted use, distribution, and reproduction in any medium, provided the original work is properly cited.

IntechOpen

IntechOpen